



Dynamical analysis of extreme precipitation in the US northeast based on large-scale meteorological patterns

Laurie Agel^{1,2} · Mathew Barlow^{1,3} · Frank Colby¹ · Hanin Binder^{4,5} · Jennifer L. Catto⁶ · Andrew Hoell⁷ · Judah Cohen⁸

Received: 5 October 2017 / Accepted: 23 April 2018
© Springer-Verlag GmbH Germany, part of Springer Nature 2018

Abstract

Previous work has identified six large-scale meteorological patterns (LSMPs) of dynamic tropopause height associated with extreme precipitation over the Northeast US, with extreme precipitation defined as the top 1% of daily station precipitation. Here, we examine the three-dimensional structure of the tropopause LSMPs in terms of circulation and factors relevant to precipitation, including moisture, stability, and synoptic mechanisms associated with lifting. Within each pattern, the link between the different factors and extreme precipitation is further investigated by comparing the relative strength of the factors between days with and without the occurrence of extreme precipitation. The six tropopause LSMPs include two ridge patterns, two eastern US troughs, and two troughs centered over the Ohio Valley, with a strong seasonality associated with each pattern. Extreme precipitation in the ridge patterns is associated with both convective mechanisms (instability combined with moisture transport from the Great Lakes and Western Atlantic) and synoptic forcing related to Great Lakes storm tracks and embedded shortwaves. Extreme precipitation associated with eastern US troughs involves intense southerly moisture transport and strong quasi-geostrophic forcing of vertical velocity. Ohio Valley troughs are associated with warm fronts and intense warm conveyor belts that deliver large amounts of moisture ahead of storms, but little direct quasi-geostrophic forcing. Factors that show the largest difference between days with and without extreme precipitation include integrated moisture transport, low-level moisture convergence, warm conveyor belts, and quasi-geostrophic forcing, with the relative importance varying between patterns.

1 Introduction

Extreme precipitation is responsible for some of the most destructive and costly, in terms of human lives and resources, natural disasters in the Northeast US (Kunkel et al. 2013). These disasters include localized flash flooding in streams due to summertime convective events, urban flooding due

to extreme rainfall and poor drainage, and widespread river flooding due to tropical cyclones and spring rains combined with snowmelt. Unfortunately, the vulnerability of this region to the effects of extreme precipitation is expected to grow, as 99th-percentile daily precipitation in the region has increased 74% from 1958 to 2010 (Groisman et al. 2013), while future winter and spring precipitation over this region, based on a range of model projections using the A2 emissions scenario, is expected to increase between 5 and 20% by the end of this century (Melillo et al. 2014). The goal of this

Electronic supplementary material The online version of this article (<https://doi.org/10.1007/s00382-018-4223-2>) contains supplementary material, which is available to authorized users.

✉ Laurie Agel
lagel48@gmail.com

¹ Department of Environmental, Earth, and Atmospheric Sciences, University of Massachusetts Lowell, One University Avenue, Lowell, MA, USA

² Intercampus Marine Science Graduate Program, University of Massachusetts Lowell, Lowell, MA, USA

³ Climate Change Initiative, University of Massachusetts Lowell, Lowell, MA, USA

⁴ Institute for Atmospheric and Climate Science, ETH Zurich, Zurich, Switzerland

⁵ Laboratoire de Météorologie Dynamique/IPSL, École Normale Supérieure, Paris, France

⁶ College of Engineering, Mathematics and Physical Sciences, University of Exeter, Exeter, UK

⁷ NOAA/ESRL Physical Sciences Division, Boulder, CO, USA

⁸ Atmospheric and Environmental Research, Lexington, MA, USA

study is to investigate the dynamical mechanisms and moisture ingredients associated with Northeast US (hereafter “Northeast”) extreme precipitation by building on previous work that identifies several large-scale circulation patterns associated with this extreme precipitation (Agel et al. 2017), and providing a first step toward being able to accurately predict and prepare for future precipitation challenges for the region.

The mechanisms by which precipitation is delivered to the Northeast depend upon location relative to the coastline. Precipitation in the coastal region is strongly influenced by extratropical storms traveling along the high-density North Atlantic storm track (Hoskins and Hodges 2002). Precipitation in the inland region, while influenced by the North Atlantic storm track as well as extratropical storms traveling across the Great Lakes region, is also orographically influenced by the Adirondack, Green, and White Mountain ranges. These different regional influences result in fewer precipitation days at coastal stations than at inland stations, but with considerably higher daily intensity at coastal stations (Agel et al. 2015). At inland stations the highest daily intensity occurs in warm months, while at coastal stations peaks in daily intensity occur in spring and fall. Extreme daily precipitation (based on top 1% daily station precipitation) varies from 30+ mm at inland locations to 70+ mm at coastal locations. For both inland and coastal locations, extreme precipitation days tend to occur embedded within multiple-day precipitation events.

Accordingly, a complete dynamical analysis of extreme precipitation in the Northeast needs to consider both synoptic-scale influences as they apply to the entire region, as well as localized and sub-regional responses to those larger-scale influences. Several researchers, as part of larger-domain or global studies, have addressed the first issue by evaluating the role of synoptic-scale influences on extreme precipitation in the Northeast. Pfahl and Wernli (2012), using 99th percentile 6-h modeled precipitation, estimated that 60–80% of extreme precipitation along the eastern US seaboard occurs near extratropical cyclone centers. Pfahl and Sprenger (2016) quantified the role of cyclone intensity and moisture availability in generating precipitation, and found that intensity and moisture scale well to precipitation, especially in low-latitudes, but that moisture availability can act as an independent factor in mid- and high-latitudes. Collopy et al. (2016) found strong anomalous moisture transport and lower sea level pressure associated with summertime Northeast cyclones for 95th percentile precipitation events. Kunkel et al. (2012), using daily precipitation exceeding a 1-in-5-year occurrence, found that Northeast extreme precipitation can be attributed in 16% of the cases to nearby extratropical cyclones, in 47% of the cases to frontal processes, and in 36% of the cases to tropical cyclones. Dowdy and Catto (2017) found that the combination of a cyclone

and a front is the most common cause of extreme precipitation (6-h 99th percentile) in the Northeast.

Several studies have further explored the relevance of fronts to precipitation. Based on global figures from Catto et al. (2012), approximately 18–30% of Northeast annual total daily precipitation is related to cold fronts, while 30–42% is related to warm fronts. However, extreme precipitation is more likely to be associated with warm fronts: Catto and Pfahl (2013) found that 40–50% of 6-h ERA-Interim extreme precipitation occurs with nearby warm fronts in the Northeast, despite the fact that only 5–10% of fronts generate extreme precipitation.

Warm conveyor belts (WCBs), well-defined moist air-streams in an extratropical cyclone’s warm sector that rise from the boundary layer into the upper troposphere (Green et al. 1966; Harrold 1973; Wernli and Davies 1997) and feature intense latent heat release (Browning 1990), are also linked to extreme precipitation. For the eastern US, Pfahl et al. (2014) showed that about 50–70% of all extreme precipitation events between 1979 and 2010 were related to WCBs. WCBs, particularly those linked to extreme precipitation, often occur in conjunction with warm and cold fronts in the Northeast (Catto et al. 2015). WCBs also play an important role for atmospheric dynamics. In the early phase of the WCB ascent, diabatic potential vorticity (PV) production leads to the formation of a positive PV anomaly (Wernli and Davies 1997), which is essential for the intensification of many strongly deepening cyclones (Stoelinga 1996; Binder et al. 2016), while in the upper troposphere diabatic PV reduction produces negative PV anomalies that can amplify upper-level ridges and influence the downstream flow evolution (Wernli 1997; Pomroy and Thorpe 2000; Grams et al. 2011).

In the current study, we build on these previous results, while also examining the sub-regional response to larger-scale synoptic forcings, by taking a detailed view of the processes related to extreme Northeast precipitation within the context of several Large-Scale Meteorological Patterns (LSMPs; Grotjahn et al. 2016). LSMPs are typically defined at a scale larger than the mesoscale but smaller than the scale of climate variability, and relate to some observed phenomena, such as precipitation or temperature extremes (e.g., Loikith and Broccoli 2012; Glisan and Gutowski 2014; Callow et al. 2016; Roller et al. 2016). Here, the LSMPs used are six previously-defined upper-level circulation patterns of dynamic tropopause height that are linked to the top 1% of daily extreme precipitation in the Northeast (Agel et al. 2017). Dynamic tropopause height is an effective field to use for large-scale pattern identification, since it provides a compact representation of the upper-level flow, as gradients of PV along the tropopause are directly related to the strength of upper-level troughs and ridges (Hoskins et al. 1985; Nielsen-Gammon 2001). For each tropopause LSMP,

we examine the associated three-dimensional large-scale circulation, as well as a range of factors relevant to precipitation, including moisture, stability, and synoptic mechanisms associated with lifting. Because the six LSMPs are linked to extreme precipitation days only, we extend our analysis by also considering six similar patterns drawn from a set of LSMPs identified for all days 1979–2008 (Agel et al. 2017). For the similar-patterned LSMPs, we compare the relative strength of the circulation and factors between days with and without the occurrence of extreme precipitation.

The paper is organized as follows. In Sect. 2, the data products and methods used to develop the tropopause patterns and to identify the key ingredients or processes related to extreme precipitation within each tropopause pattern are described. In Sect. 3, the tropopause LSMPs are described and a set of composite figures showing key circulation fields, moisture fields, instability measures, and synoptic mechanisms for each set of pattern days, as well as the differences between several of these fields on extreme vs. non-extreme days, are used to examine how these factors relate to extreme precipitation within each LSMP. In Sect. 4 we provide a summary of our results (including a summary schematic of how circulation, moisture, and instability contribute to extreme precipitation within each of our tropopause patterns), as well as further discussion regarding the role of moisture transport, and a brief discussion of future work.

2 Data and methods

2.1 Extreme precipitation days

Northeast extreme precipitation is identified as the top 1% of daily precipitation exceeding 0.01 in, or 0.254 mm, at 35 United States Historical Climatology Network (USHCN; Easterling et al. 1999) stations for the years 1979–2008, as developed in Agel et al. (2015). Each station is missing no more than 1% of the daily values. Extreme days related to tropical cyclones, defined as days where a station experiencing extreme precipitation is within 1000 km of a HURDAT2 (Landsea and Franklin 2013) tropical cyclone track, are eliminated, leaving a total of 691 unique dates with non-tropical cyclone-related extreme precipitation at one or more stations. The station locations, regional variation of top 1% threshold values, and seasonal frequency of the extreme dataset are shown in Online Resource 1, reproduced from Agel et al. (2015), where the division of coastal and inland stations runs roughly along the 45 mm day⁻¹ threshold contour. The seasonal categories used here and throughout the paper are December–February (DJF), March–April (MAM), June–August (JJA), and September–November (SON). The National Oceanic and Atmospheric Administration (NOAA) Climate Prediction Center (CPC) 0.25° × 0.25° Daily U.S.

Unified Precipitation (CPCU; Chen et al. 2008) is also used to show region-wide precipitation, and is provided by NOAA/OAR/ESRL PSD (<http://www.esrl.noaa.gov/psd/> <http://www.esrl.noaa.gov/psd/data/gridded/data.unified.daily.conus.html>).

2.2 Dynamic tropopause patterns

The six tropopause LSMPs, previously identified in Agel et al. (2017), are created by applying k-means clustering (KMC; Diday and Simon 1976; Michelangeli et al. 1995) to daily standardized anomalies of dynamic tropopause height for the 691 extreme precipitation days defined above. The standardized anomaly fields are created from daily means of the National Aeronautics and Space Administration (NASA) Modern Era Retrospective Reanalysis for Research and Application (MERRA, Rienecker et al. 2011) blended tropopause height (provided in units of pressure, at 1-h intervals on a 2/3° × 1/2° grid). This field is a smoothed mix of PV-based tropopause pressure at higher latitudes and temperature-based tropopause pressure at lower latitudes. Because we use MERRA's blended approach to defining the tropopause height, we use the terms “dynamic tropopause height” and “tropopause pressure” interchangeably here. The standardized anomalies are produced by removing the long-term daily mean from the daily mean at each grid point, and dividing the result by the temporal standard deviation of the values at the grid point. The long-term daily mean is created at each grid point by taking a 30-year mean of each calendar day and smoothing the results with a 21-day running mean.

In addition to KMC typing on extreme precipitation days, Self-Organizing Maps (SOMs, Kohonen 2001) of dynamic tropopause height for all days 1979–2008, previously developed in Agel et al. (2017), are used to identify the differences between extreme precipitation days and non-extreme precipitation days within each SOM pattern. The SOM technique applies unsupervised learning to neural network classifications, to create a number of distinct “nodes”, or patterns, for an input field. Here, the input field is identical to the dynamic tropopause height field used for the KMC analysis, and the SOM algorithm is specified to use linear initialization, 200 initial training iterations, 1200 secondary training iterations, and a 5 × 6 rectangular pattern space with an initial training radius of 6. A complete description of the KMC and SOM methods used to create the tropopause LSMPs is available in Agel et al. (2017).

2.3 Additional reanalysis variables

We use additional MERRA reanalysis data to evaluate the key dynamical fields and physical properties associated with the extreme precipitation-producing circulation patterns. 200-hPa winds, 500-hPa geopotential heights, mean

sea level pressure (MSLP), and 700-hPa vertical velocities are used to identify the three-dimensional circulation associated with each LSMP. Lowest model level winds and specific humidity are used to show low-level moisture convergence (LLMC), which can enhance precipitation amounts above that expected from a simple Clausius–Clapeyron perspective (Muller et al. 2011). Integrated vapor transport (IVT) is used to provide a measure of moisture flux into the region. The static stability parameter for an isobaric system, calculated at 750 hPa from temperature and pressure per Eq. 3.7 in Holton (2004), is used to show areas where buoyancy can enhance precipitation production. Ertel’s PV (EPV), for the 900–100-hPa layer, is used to show vertical cross-sections where lift may be enhanced by diabatic heating, particularly due to the release of latent heat during precipitation. The thermal wind form of quasi-geostrophic (QG) forcing (right-hand-side of Eq. 6.36 in Holton 2004), specifically the advection of 700-hPa geostrophic relative vorticity by the 900–500 hPa thermal wind¹, is used to identify areas where synoptic mechanisms such as temperature advection and vorticity advection may play a role in generating lift. The MERRA data is at two different resolutions – geopotential heights, temperature, MSLP, horizontal winds, EPV, specific humidity, and vertical velocity are provided at 3-h intervals on a $1.25^\circ \times 1.25^\circ$ grid; while IVT and other single-level fields are available at 1-h intervals on a $2/3^\circ \times 1/2^\circ$ grid. Unless otherwise noted, the MERRA data is evaluated at 12 UTC.

Convective Available Potential Energy (CAPE) from NOAA’s National Centers for Climate Prediction (NCEP) Climate Forecasting System Reanalysis (CFSR; Saha et al. 2010), a high-resolution coupled atmosphere-ocean-land surface-sea ice system, is used to show regions of potential convection². The field is available at 6-h intervals on a $0.5^\circ \times 0.5^\circ$ grid. Here we use the 18 UTC field, as CAPE values for the Northeast tend to peak from 18 to 22 UTC (based on manual inspection for the dates considered).

Anomalies of all reanalysis fields are calculated by subtracting the smoothed long-term daily means at each grid point from the 12 UTC (unless otherwise noted) fields. The long-term daily means are calculated as for MERRA tropopause height.

¹ The 900–500 hPa layer is chosen as opposed to the more familiar 1000–500 hPa layer because MERRA does not include interpolated values below the lowest model sigma level, resulting in many missing values at 1000 hPa for the Northeast.

² The CFSR CAPE field is used instead of calculation directly from MERRA due to the lack of MERRA interpolated values below 900 hPa for the Northeast.

2.4 Storm tracks

Storm track data is derived by applying the tracking algorithm of Hoskins and Hodges (2002) to 6-h European Center for Medium-range Weather Forecasting (ECMWF) ERA-Interim (Dee et al. 2011) 850-hPa relative vorticity with a methodology similar to Catto et al. (2010). The vorticity field is spectrally truncated at 42 wavenumbers (T42) to eliminate small-scale features, and further filtered to remove wavenumbers $n \leq 5$ before identification of vorticity maxima. Tracks are established from the maxima using a nearest neighbor approach, from which the smoothest set of tracks, based on minimizing a cost function, are selected. The tracks are further filtered to those with duration of at least 2 days and propagation distance of at least 1000 km.

The storm track data is used to identify extreme station precipitation as storm-related (non-storm-related) if the station experiencing precipitation is within (outside of) 800 km of a storm center on the day of precipitation. The 800-km threshold is based on a manual review of station precipitation and nearby storm tracks, and is used to capture the majority of storm-related dynamics, but does not necessarily include precipitation related to elongated fronts far removed from storm centers, or that due to other mechanisms such as localized convection and mesoscale convective complexes (MCCs).

2.5 Fronts

Cold and warm fronts are identical to those used in Catto et al. (2012), Catto and Pfahl (2013), and Catto et al. (2014). The fronts are derived from ECMWF ERA-Interim reanalysis, using an objective identification algorithm from Berry et al. (2011) to identify organized locations where a selected thermal front parameter (based on 850 hPa wet bulb potential temperature) is lower than a specified negative threshold value. Fronts are then placed where the gradient of the thermal front parameter is zero (Hewson 1998). The fronts are identified as warm or cold based on overall speed and direction, and are provided on a $2.5^\circ \times 2.5^\circ$ grid at 6-h intervals.

Frontal density at each grid box is calculated per day based on the number of times a front is present in each grid box (0–4 counts per day). The densities are calculated in a station-relative manner (that is, the front positions are shown in relation to the location of the stations experiencing extremes). In this case, for each extreme precipitation day (which may feature extreme precipitation at more than one station), the nearest frontal grid location is found for each station experiencing extreme precipitation, and a surrounding 35° latitude \times 40° longitude box (with the station in the center) is used to gather the station-relative frontal density. Station-centric frontal density on an extreme day is then calculated as the mean of these $35^\circ \times 40^\circ$ station-relative frontal

densities. In addition, Online Resource 2 shows the actual composite location of the fronts for storm-related and non-storm-related days, as well as the station-centric warm and cold fronts separated by coastal and inland station extremes.

2.6 Warm conveyor belts

WCBs are obtained from the global climatology of Madonna et al. (2014), based on 6-h ECMWF ERA-Interim reanalysis fields evaluated at 60 vertical levels and interpolated onto a $1^\circ \times 1^\circ$ longitude-latitude grid. WCB trajectories are calculated with the trajectory tool LAGRANTO (Wernli and Davies 1997; Sprenger and Wernli 2015). At each 6-h time step, three-dimensional kinematic 2-day forward trajectories are started from an equidistant grid in the lower troposphere (between 1050 and 790 hPa) with a horizontal spacing of 80 km and a vertical spacing of 20 hPa. Trajectories that ascend more than 600 hPa within 2 days in the vicinity of an extratropical cyclone are then classified as WCB trajectories (see Madonna et al. 2014 for details). Analogous to Binder et al. (2016), low- and upper-level WCB trajectory frequencies are defined at each grid point as the percentage of pattern days associated with at least one WCB air parcel with $p > 500$ hPa and $p < 500$ hPa, respectively, at the grid point at 12 UTC.

2.7 Statistical significance

Statistical significance, unless noted otherwise, is established through a Monte Carlo approach, in which the pattern assignments are randomly shuffled (among the 691 days for the KMC clusters, or among all days for the SOM patterns), and the desired quantity (for example, seasonal frequency of the KMC pattern dates) is recalculated. This process is repeated 1000 times, creating a range of values. A quantity is considered statistically significant if it falls below the bottom 2.5% or above the top 97.5% of the randomly generated values.

2.8 Comparison of fields between extreme and non-extreme days

Differences between extreme-precipitation days and non-extreme precipitation days within each LSMP are explored for select fields using the all-days SOM patterns most similar to the KMC patterns. To identify these differences, each of the KMC patterns must also occur in the all-day SOM context, and the SOM patterns most similar to the KMC patterns must explain the majority of extreme precipitation. Online Resource 3, reproduced from Agel et al. (2017), shows the tropopause SOM patterns, the frequency of extreme precipitation days represented by each SOM pattern, and the frequency of KMC pattern days C1–C6 represented by each

SOM pattern. The SOM patterns most representative of the C1–C6 patterns and used in this paper are SOM4, SOM26, SOM13, SOM8, SOM20, and SOM1, respectively.

For each field, the non-extreme-day composite is subtracted from the extreme-day composite, and the results are standardized at each grid point by subtracting the grid point mean and dividing by the grid point temporal standard deviation. This allows a comparison of the relative strength of the fields' differences, independent of the units of the original fields. Only statistically significant differences at the 0.05 level as defined through Monte Carlo resampling are considered.

3 Results

The six tropopause LSMPs (Agel et al. 2017) are reproduced here in Fig. 1a, along with the seasonal frequency of the patterns (Fig. 1b), and the location of precipitation and extreme precipitation events within each pattern (Fig. 1c). The patterns represent three basic tropopause configurations: a ridge over the Northeast, a trough along the eastern US, and a trough over the Ohio Valley. The six-pattern set of LSMPs includes two distinct ridge patterns (C1 and C4, together representing over 44% of the extremes), two seasonal variations of the eastern trough (C2 and C5), and two seasonal variations of the Ohio Valley trough (C3 and C6). The remainder of this section will address each of the ridge patterns separately, followed by an analysis of the eastern troughs together, and finally an analysis of the Ohio Valley troughs together.

3.1 Ridge pattern C1

The C1 pattern features an anomalously high tropopause ridge spread across the eastern US (Fig. 1a). Although extreme precipitation can occur anywhere in this pattern, it occurs most often along the Canadian/New England border during JJA (Fig. 1b, c). However, overall precipitation is light, suggesting localized processes for extreme precipitation. The pattern is associated with predominantly westerly flow at mid- and upper-levels (Fig. 2a, b) and widespread anomalously low MSLP to the west of the region (Fig. 2c). There is widespread slightly anomalous upward motion (approximately -0.5 Pa s^{-1} , consistent through a deep layer of the air column) at grid scale (Fig. 2d). There are regions with low-level moisture convergence (LLMC) anomalies, particularly to the northwest along the Great Lakes (Fig. 2e), and anomalously high IVT values extending from the Ohio Valley into the interior Northeast (Fig. 2f). These anomalies are often in place at least 48 h before extreme precipitation occurs (not shown). Static stability (Fig. 2g) is anomalously low for the entire pattern, but is especially low in western

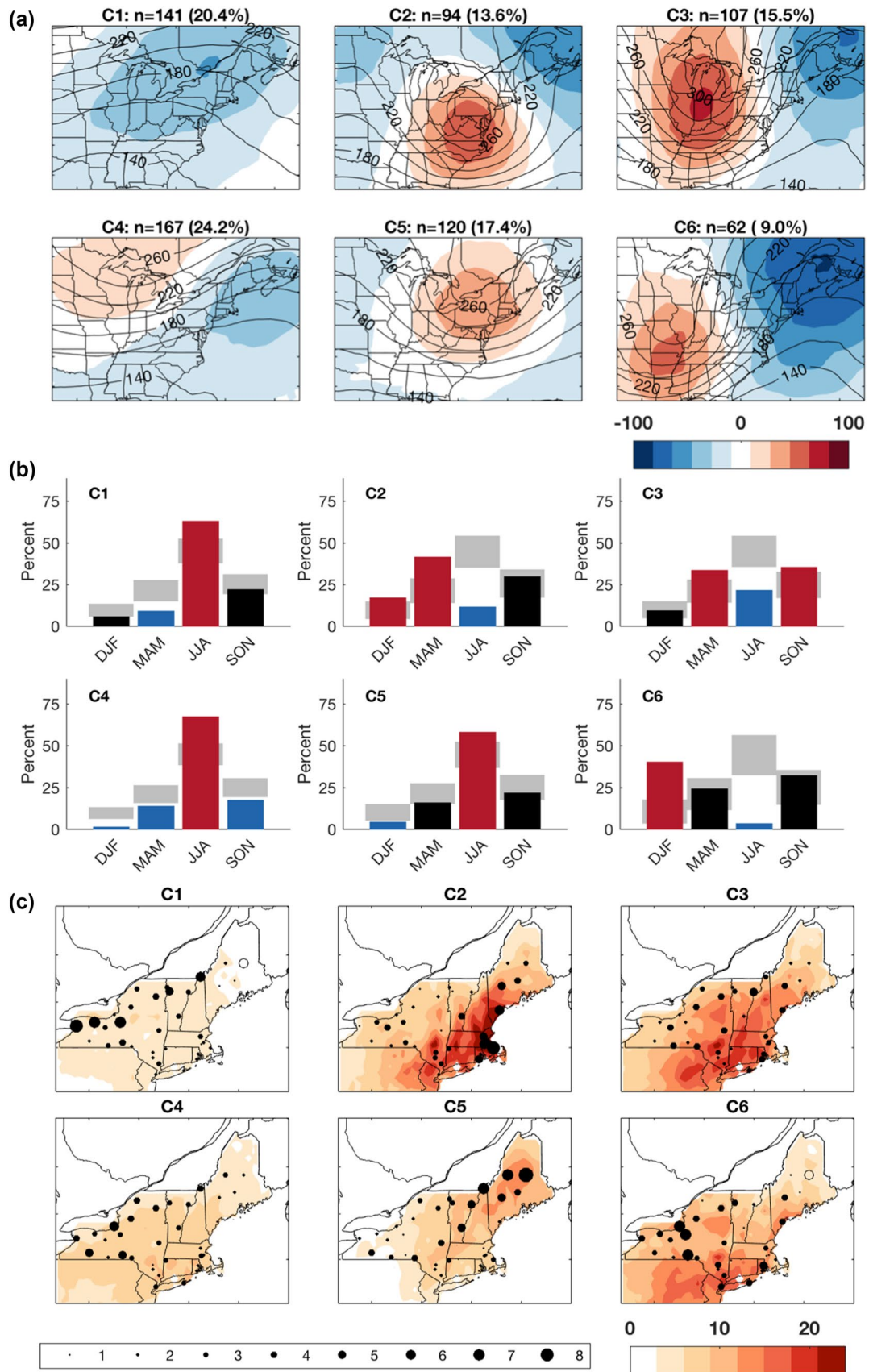


Fig. 1 Results of k-means separation of MERRA blended tropopause height anomalies for 691 top 1% extreme precipitation days, 1979–2008, into six patterns C1–C6, showing **a** composites of tropopause pressure (contours, in 20 hPa intervals, and anomalies, shaded), **b** seasonal frequency (expressed as a percent) of each pattern (red if greater than that expected due to chance, blue if less than that expected due to chance, black otherwise), and **c** the percentage of pattern days accounted for by extremes at each station (black dots, with size proportional to percentage, ranging from 0 to 8%), overlaid on CPCU gridded precipitation anomaly composite for each pattern (shaded, mm). The text above each pattern in **a** indicates the number of dates in each composite. The significance in **b** is based on 95% confidence interval using Monte Carlo sampling (shown as grey boxes). Anomalies calculated by subtracting 30-year smoothed daily mean from daily values. Figure reproduced from Agel et al. (2017)

New York, where LLMC and IVT are largest. The warm moist air mass and weak synoptic-scale forcing suggests that convection plays an important role in extreme precipitation production for this pattern. This is supported by the CAPE anomalies in Fig. 2h, which are the highest and most widespread of the six patterns for the Northeast region.

While organized convection is likely a key factor in these extremes, a more complex situation is revealed when nearness to storm tracks and surface fronts are explored. Although the storm track density is the weakest of the six patterns, and, accordingly, the percent of storm-related extremes is the lowest for the six patterns (Table 1), still more than 70% of the extremes in this pattern are storm-related, suggesting the important role of synoptic-scale triggering of mesoscale processes. However, anomalies for storm-related fields, such as QG forcing (Fig. 2i), WCBs (Fig. 2j), and EPV (Fig. 2k) are very small, indicating that storms in this pattern are likely weak and shallow.

For both storm-related and non-storm-related extremes, warm fronts tend to be located nearby (Fig. 2l). Cold fronts also appear nearby to stations experiencing non-storm-related extremes. These cold fronts may be associated with distant storm centers, or they may be surface fronts caused by other mechanisms such as cold pools and mesoscale convective system outflows (Schumacher and Johnson 2005). The frontal patterns may also be consistent with small frontal-wave cyclones spinning up on trailing cold fronts, which could explain the presence of cold fronts to the northeast of the stations and the high frequency of warm fronts in the non-storm related composites.

Thermal fronts can be initiated by shortwaves passing through a ridge environment. Figure 2c shows a composite “kink” in the MSLP over the Great Lakes, which could reflect a surface response to shortwaves. Although the composite 500-hPa heights do not show this, many of the individual 500-hPa height maps do show evidence of shortwaves in the overall flow. This is consistent with the findings of Milrad et al. (2014), who found that vorticity maxima propagating through longwave ridges often provided a

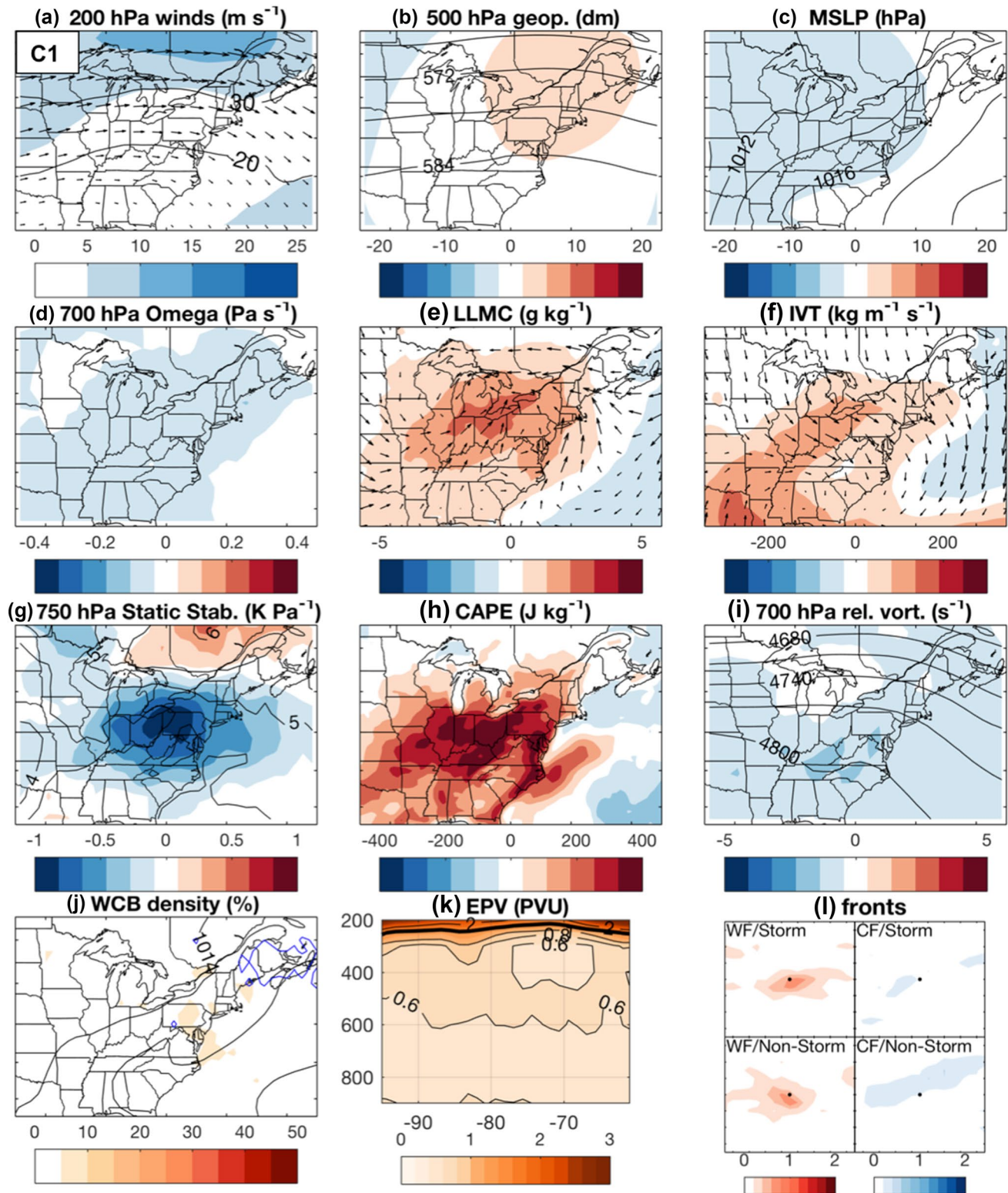
warm-season trigger for convection in Montreal. The presence of anomalous LLMC in western New York may also provide some evidence of shortwave activity and attendant surface circulation. In Fig. 3 we composite station-relative MERRA 500-hPa geopotential heights for the C1 pattern on the higher-resolution $2/3^\circ \times 1/2^\circ$ grid, separated into storm-related and non-storm-related extremes. There is a noticeable shortwave in the composite pattern for storm-related extremes, along with an area of positive relative vorticity, which is not present for the non-storm-related extremes, confirming that at least some of the precipitation extremes in this pattern may be related to shortwaves and their attendant surface disturbances.

Many of the circulation features and moisture variables in this pattern occur on non-extreme precipitation days as well, based on similar patterns in the all-day SOM analysis. However, the ingredients most important for generating extreme precipitation as opposed to ordinary precipitation in the C1 pattern include surface lows (possibly due to shortwaves) over western New York (Fig. 4b), moisture availability due to strong southwesterly IVT and LLMC (Fig. 4c, d), and convection in regions of relatively high CAPE (Fig. 4f).

3.2 Ridge/trough C4

Like C1, the C4 pattern features an anomalously high tropopause ridge over the Northeast, but unlike C1, the C4 ridge is part of a shallow tropopause ridge/trough couplet located across the eastern US (Fig. 1a). This pattern is also similar to C1 in seasonality (mostly JJA; Fig. 1b), precipitation features (widespread light precipitation), and location of extremes (more extremes inland and to the northwest; Fig. 1c). Upper- and mid-level circulation fields (Fig. 5a, b) also mirror the tropopause trough/ridge, with a widespread area of anomalously low MSLP (Fig. 5c) across the Northeast. There is slightly more upward vertical motion (Fig. 5d) than for pure ridge C1, possibly aided by a 200-hPa jet streak over northern New England, but overall upward motion is not particularly extreme, except in localized pockets. Surface heating is strong over coastal regions, with a thermal boundary along northern and western New England separating cooler air to the north (not shown). Despite extremes occurring more frequently inland, localized pockets of heavy precipitation also occur along the coast, where moderate moisture availability, in terms of LLMC (Fig. 5e) and IVT (Fig. 5f), is present. Like C1, static stability is anomalously low (Fig. 5g), and convection appears to be associated with some of the extremes, particularly in New York (Fig. 5h).

QG forcing (Fig. 5i) is moderate over regions with high numbers of extremes (western New York), consistent with the enhanced frequency of inland storms (Table 1). Coastal regions contain areas of weak WCB density (Fig. 5j), and slightly elevated EPV at low levels (Fig. 5k). Cold and warm



fronts are associated with both storm-related and non-storm-related extremes (Fig. 5l). This indicates that at least some of the storm-related extremes in coastal regions are linked to WCBs ascending over the warm or cold fronts of the

associated storms. Otherwise the pattern is consistent with relatively weak synoptic systems at inland locations, or trailing cold fronts associated with remote cyclones to the north-east. The key factors linked to extreme precipitation in this

Fig. 2 Composite fields for ridge pattern C1 days, showing **a** 200-hPa wind magnitude (m s^{-1} , contours and shaded anomalies) and direction (arrows), **b** 500-hPa geopotential height (dm, contours and shaded anomalies), **c** MSLP (hPa, contours and shaded anomalies), **d** 700-hPa vertical velocity anomalies (Pa s^{-1} , shaded), **e** LLMC, represented by lowest model-level wind anomalies (m s^{-1} , arrows) and lowest model-level specific humidity anomalies (g kg^{-1} , shaded), **f** IVT magnitude ($\text{kg m}^{-1} \text{s}^{-1}$, contours and shaded anomalies) and direction (arrows), **g** 750-hPa static stability (K Pa^{-1} , contours and shaded anomalies), **h** CFSR CAPE (J kg^{-1} , shaded anomalies) at 18 UTC, **i** QG forcing based on thermal wind formulation, i.e. 700-hPa relative vorticity (10^{-5}s^{-1} , shaded) advection by the 900–500 hPa thermal wind (isotherms of 900–500 thickness, m, are shown to indicate thermal wind direction), **j** WCB trajectory frequency, i.e. percentage of extreme precipitation days associated with at least one WCB at each grid point (below 500 hPa, color shading, and above 500 hPa, blue contours for 5, 10, 20, 30, 40 and 50%), potential vorticity at 315K (thick black contours for 2, 3 and 4 PVU), and MSLP (black contours every 3 hPa), **k** Ertel's PV anomaly cross-sections (shaded, PVU) at 43°N for 900–200 hPa, and **l** density of warm fronts (red shading) and cold fronts (red shading) relative to stations experiencing extreme precipitation (black dot in center of 40° longitude \times 36° latitude grid), separated into storm-related (within 800 km of Era-Interim storm track based on 850-hPa relative vorticity) and non-storm-related extremes. Unless otherwise noted, all fields are from MERRA and evaluated at 12 UTC

pattern, as opposed to ordinary precipitation, are enhanced moisture transport due to IVT and LLMC along the coast (Fig. 6c, d), the presence of WCBs near the coast (Fig. 6e), and slightly elevated CAPE in southern regions (Fig. 6f).

3.3 Eastern troughs C2 and C5

The C2 and C5 patterns feature tropospheric troughs across the eastern US. The C2 trough axis extends from the Great Lakes through the Carolinas, with a slight negative tilt and a closed or nearly closed upper-level low (Fig. 1a). The C5 pattern is both shallower and shifted slightly farther east than C2, and unlike C2, features a slight progressive tilt (Fig. 1a). The C2 pattern occurs preferentially during DJF and MAM, while the C5 pattern occurs preferentially during JJA (Fig. 1b). Unlike the other patterns, the stations experiencing the highest number of extremes in these patterns are located along the eastern seaboard – to the extreme southeast for C2, and in Maine for C5 (Fig. 1c). The composite daily precipitation intensity in C2 is the strongest of the patterns (71.2 mm day^{-1}).

Over 90% of the extreme days in C2 are associated with nearby storms (Table 1), with roughly 2/3 of the storm-related extremes occurring at coastal stations. Composite circulation shows an absence of jet streaks (Fig. 7a), a nearly closed mid-level circulation with a slightly regressive tilt (Fig. 7b), and a well-defined surface low with central pressure that is the lowest of the six patterns (Fig. 7c). There is a strong thermal gradient between an anomalously cool Ohio Valley and an anomalously warm Northeast (not shown).

Upward motion anomalies are among the highest of the patterns (Fig. 7d), peaking at nearly -1.0 Pa s^{-1} around 750 hPa. The pattern also features strong coastal LLMC (Fig. 7e), along with enhanced south-southeast moisture transport over the relatively warm Western Atlantic (Fig. 7f), beginning up to 48 h before the extreme event. Overall static stability is very low along the immediate coast (Fig. 7g), but CAPE is not anomalously high (Fig. 7h). Consequently, QG forcing appears to be the dominant mechanism in C2 for lift, and is in fact the strongest of the six patterns (Fig. 7i). There is also relatively frequent WCB ascent (Fig. 7j) at the upstream edge of the upper-level disturbance (although this is mostly located offshore). EPV is enhanced at low levels in the regions experiencing extreme precipitation (Fig. 7k), indicating that diabatic heating may provide a positive feedback mechanism for additional lift in this pattern. For storm-related extremes, the most frequent frontal mechanism for lift appears to be attendant warm fronts (Fig. 7l). Based on the above composite features, the C2 pattern is consistent with many of the features of traditional nor'easters (Maglaras et al. 1995; Kocin and Uccellini 2004), unusually strong storms that form along the Mid-Atlantic coastline and travel north through or near to New England along a dense track location off the New Jersey/Southern New England coast.

For the summertime C5 pattern, mid- and upper-level circulation is more open and progressive than for the wintertime C2 pattern (Fig. 8a, b). Like C2, the extremes in this pattern have a high likelihood to be storm-related (Table 1). The composite surface low is located along the Maine coast (Fig. 8c), where the highest-intensity precipitation occurs (Fig. 1c). Storms in this pattern tend to track from southern Ontario towards southeastern New England before moving northeast through Maine (not shown). Lift is noticeably weaker in this pattern than for C2 (Fig. 8d), except along the Maine coast. This is a rather dry pattern throughout the rest of the region, as the anomalous moisture flow for both LLMC and IVT is from the north (Fig. 8e, f). However, there is weak instability (Fig. 8g), and slightly enhanced CAPE at inland locations (Fig. 8h). In addition, there is moderate QG forcing throughout the region (Fig. 8i), but only weak WCB frequency located offshore (Fig. 8j), and no notable diabatic heating suggested by the EPV cross-section (Fig. 8k). Fronts appear to be too far from station locations to provide triggering mechanisms, except in the case of non-storm-related cold fronts (Fig. 8l), especially at inland stations. In these cases, the cold fronts are located both to the southwest and northeast of the station location, suggesting that some extremes may be related to remote cyclones with trailing cold fronts. Hence in this pattern the inland extremes may be associated with both direct QG forcing from weak storms and lift associated with trailing cold fronts; while the coastal extremes may be associated with direct QG forcing

Table 1 Relative frequency (%) of select categories within each pattern type C1–C6

Category	C1	C2	C3	C4	C5	C6
Coastal	27.1 (L)	63.7 (H)	43.2	33.3 (L)	40.0	40.9
Inland	72.9 (H)	36.3 (L)	56.8	66.7 (H)	60.0	59.1
Storm-related	70.3 (L)	90.7 (H)	76.8	77.9	88.7 (H)	80.3
Non-storm-related	29.7 (H)	09.3 (L)	23.2	22.1	11.3 (L)	19.7
Coastal/storm	22.7 (L)	59.1 (H)	29.2	25.5 (L)	38.0	31.4
Coastal/non-storm	04.4	04.7	14.0(H)	07.9	02.1 (L)	09.5
Inland/storm	47.6	31.7 (L)	47.6	52.4 (H)	50.8	48.9
Inland/non-storm	25.3 (H)	04.6 (L)	09.2	14.2	9.23	10.2

Categories are based on station location (coastal or inland) and nearness (within 800 km) to Era-Interim storm tracks on day of extreme precipitation. Frequencies higher (lower) than expected due to chance are followed by an “H” (“L”), based on Monte Carlo resampling

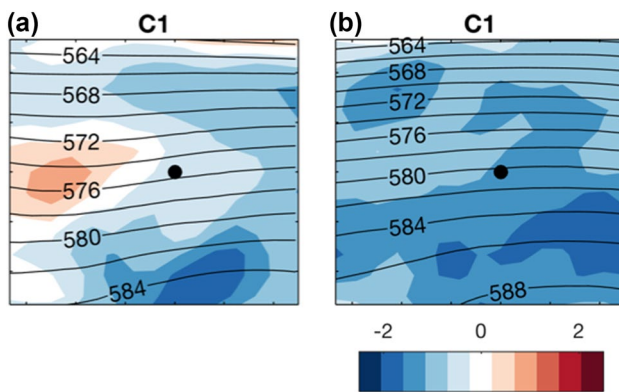


Fig. 3 500-hPa geopotential height (dm) and relative vorticity (10^{-5} s^{-1} , shaded), relative to stations experiencing extreme precipitation (black dot in center of 40° longitude \times 36° latitude grid) for **a** storm-related extreme precipitation, and **b** non-storm-related extreme precipitation for ridge pattern C1

by stronger storms, and possibly southerly moisture transport in offshore WCBs and warm fronts.

Although C2 and C5 differ in some respects, the key elements that distinguish extreme precipitation-producing days from non-extreme precipitation-producing days are very similar. These include enhanced tropospheric ridging over southeastern Canada (Figs. 9a, 10a), a well-defined storm track with more intense storms (Figs. 9b, 10b), and stronger southerly moisture feed embedded in WCBs (Figs. 9d, e, 10d, e); but notably do not include enhanced QG forcing in the regions experiencing the highest number of extremes (Figs. 9f, 10f).

3.4 Ohio Valley troughs C3 and C6

The Ohio Valley trough patterns C3 and C6 represent the deepest tropopause troughs associated with Northeast extreme precipitation, with trough axes extending from the western Great Lakes through the southern US states. C3

represents the deepest troposphere trough (Fig. 1a), and is common in MAM and SON (Fig. 1b); while the C6 trough is both slightly shallower and shifted farther west than its C3 counterpart (Fig. 1a), and occurs preferentially in DJF (Fig. 1b). The C6 pattern, featuring the strongest ridging of the six patterns (concentrated over southeastern Canada), is the least frequent of the six patterns (only 9% of extreme precipitation days fall into this category). There is widespread anomalously intense precipitation over the entire region for C3, and over more southerly regions for C6 (Fig. 1c).

Large-scale circulation is similar for both patterns (but more pronounced for C6), with jet streaks over extreme northern New England (Figs. 11, 12a), well-defined anomalous 500-hPa troughs and ridges (Figs. 11, 12b), and surface lows tracking across inland portions of the eastern US (Figs. 11, 12c). In general, however, the composite surface lows for C3 and C6 are not as deep as those for the C2 pattern. The Northeast is wedged between anomalously cold and warm air masses (not shown), and there is strong lift over the Northeast (Figs. 11, 12d). Enhanced LLMC is concentrated along the southeast coast (Figs. 11, 12e), and IVT (Figs. 11, 12f) is the strongest of the patterns, with anomalously high values extending from the Florida coast into interior New England. QG forcing is present for western locations in C6 and throughout most of the domain for C3 (Figs. 11, 12i), but the forcing is weaker than that for C2 and C5. However, the frequency of WCBs (Figs. 11, 12j), especially for C6, is the highest of the patterns. In addition, anomalously high EPV values are present throughout the cross section (Figs. 11, 12k), hinting at intense latent heating within the ascending WCB airstreams. Warm fronts are near to stations experiencing extremes (Figs. 11, 12l), for both storm-related and non-storm-related precipitation, and at both inland and coastal stations. For non-storm-related extremes, cold fronts may also accompany extremes, especially for inland locations.

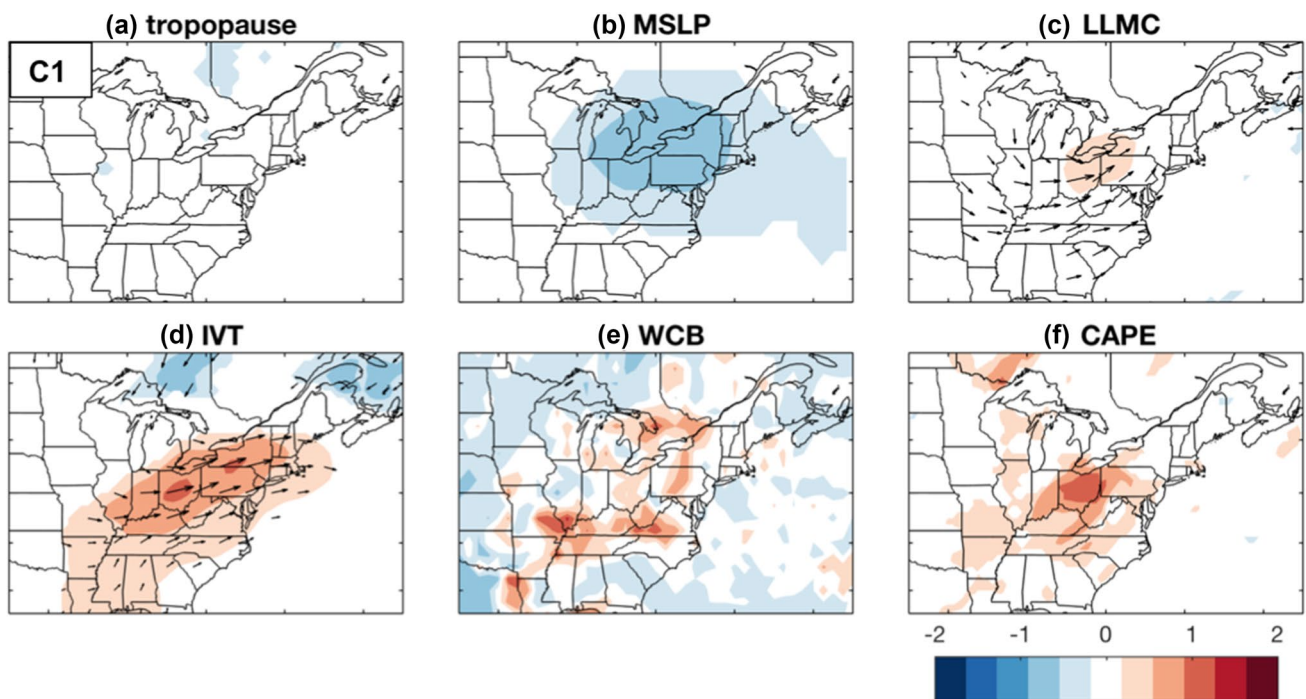


Fig. 4 Extreme day composite minus non-extreme day composite for SOM4 (similar to C1), showing differences in standardized **a** tropopause height anomalies, **b** MSLP anomalies, **c** LLMC anomalies, **d** IVT anomalies, **e** WCB frequencies, and **f** CAPE anomalies. The

fields are standardized before differencing by dividing by the temporal standard deviation. Only differences significant to the 0.05 level are shown

Despite the cohesiveness of the WCB high-frequency locations in relation to the areas experiencing extremes, there is no well-defined storm track, but rather a loose cluster of tracks over the region for C3, and a smaller cluster of tracks to the south of New York and Connecticut for C6 (not shown). This stands in sharp contrast to the C2 pattern, where most extremes feature surface lows tracking in the same area along the eastern seaboard. Accordingly, extreme precipitation in these patterns is likely linked, at least in part, to the strength (intensity of ascent) of the WCBs, which are linked to the strong QG forcing to the west of the domain (where the surface lows are positioned). Overall, although the C3 and C6 patterns share many similar features, the higher intensity of the C6 dynamical and moisture factors (particularly WCBs) appears to be linked to and mirrored by the enhanced tropospheric ridging over eastern sections. This enhanced ridging is most likely related to the net cross-isentropic transport of low-PV air into the tropopause region within the WCBs, resulting from the destruction of PV above the diabatic heating maximum (Wernli and Davies 1997; Grams et al. 2011). Not surprisingly, extreme precipitation in these patterns, versus ordinary precipitation, is more likely to feature tropospheric ridging (Figs. 13a,

14a), strong southerly IVT (Figs. 13d, 14d), and WCBs (Figs. 13e, 14e).

4 Summary

Previously, six large-scale meteorological patterns (LSMPs) of dynamic tropopause height associated with extreme precipitation in the Northeast were identified by Agel et al. (2017). In this study, we examine the three-dimensional structure associated with these LSMPs, in terms of circulation patterns and factors relevant to precipitation, including moisture, stability, and synoptic mechanisms associated with lifting. Within each pattern, the link between the different factors and extreme precipitation is further investigated by comparing the relative strength of the factors between days with and without the occurrence of extreme precipitation. The relevant factors linked to extreme precipitation differ among the patterns, but in general include abundant moisture from integrated vapor transport (IVT) and low-level moisture convergence (LLMC) acting in the presence of synoptic-scale mechanisms for ascent, such as frontal boundaries and warm conveyor belts (WCBs) associated with extratropical storms. In Fig. 15 we summarize and

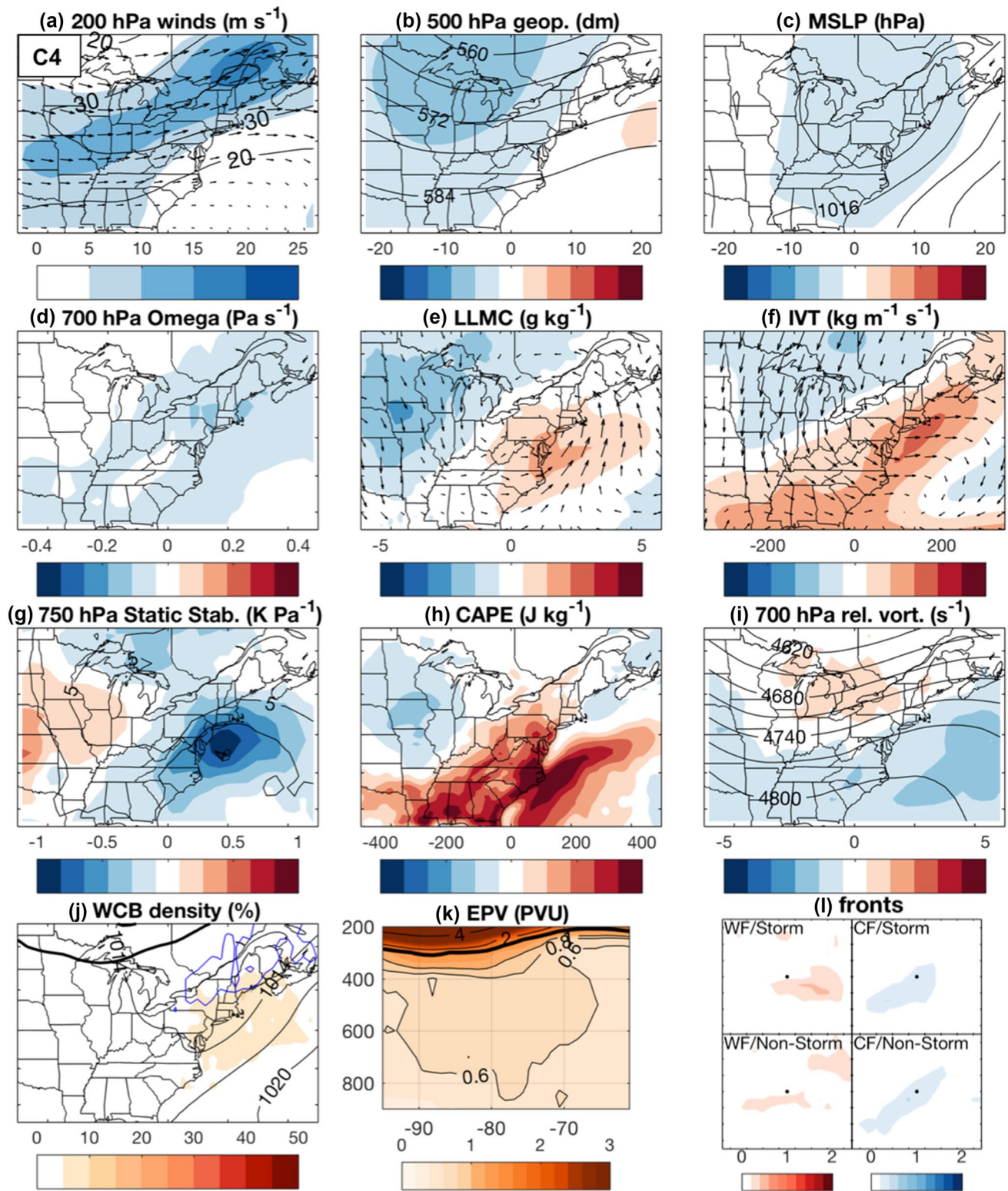


Fig. 5 Same as Fig. 2, but for trough/ridge pattern C4

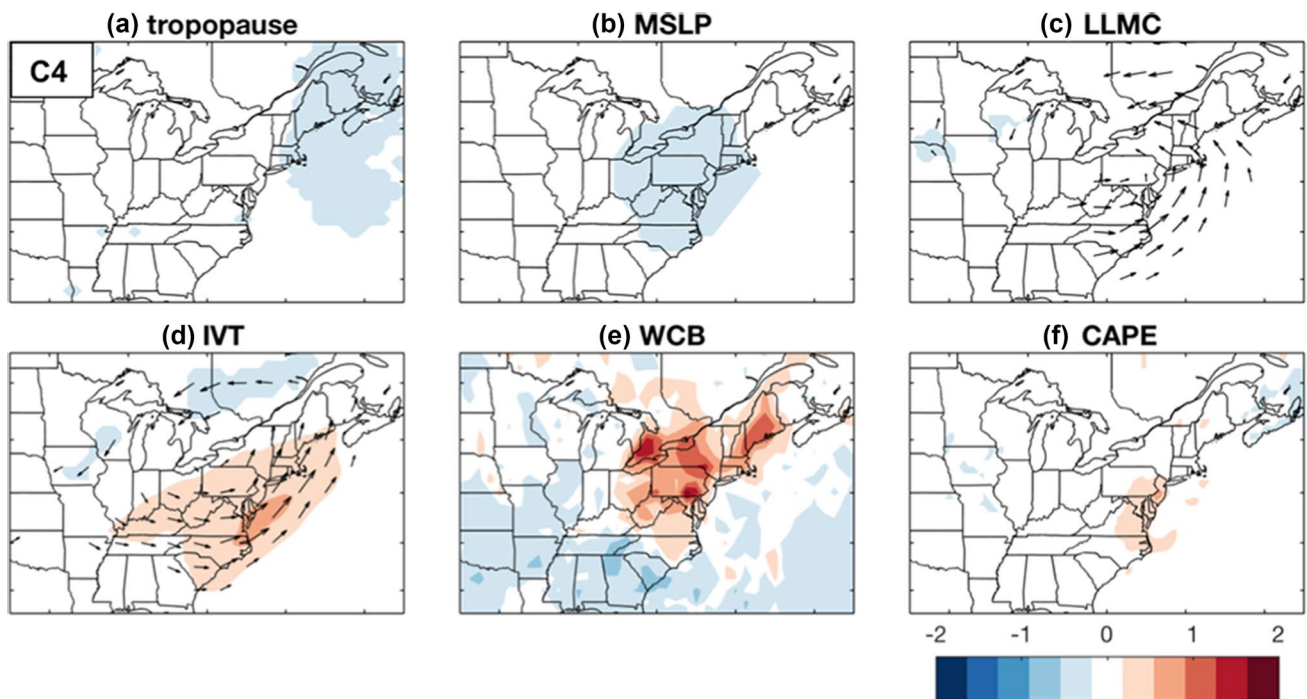


Fig. 6 Same as Fig. 4, but for SOM8 (similar to C4)

outline the dominant mechanisms for extreme precipitation for each of the patterns.

The LSMPs include a ridge pattern (C1), a shallow trough/ridge pattern (C4), two seasonal variations of “eastern troughs” (C2, C5) and two seasonal variations of “Ohio Valley” troughs (C3, C6). The ridge and trough/ridge patterns are significant in that they represent nearly 45% of the extreme precipitation days, but the precipitation in these patterns is often not directly associated with nearby synoptic storms. In contrast, the other patterns are more directly linked to synoptic dynamics. For example, the eastern trough patterns feature extreme precipitation that occurs near synoptic storms nearly 90% of the time.

Extreme precipitation occurring in conjunction with a widespread tropopause ridge in the Northeast (C1) appears to be generated by a number of processes. Precipitation under these ridges is generally light at the grid level, suggesting localized extremes. Although these extremes can occur at any station, they more commonly occur inland along the New York/Canadian border. Consistent factors associated with these extremes include anomalous moisture feed (IVT) from the Great Lakes, sometimes remaining in place for several days leading up to the extreme event, and enhanced LLMC. Potential for convective activity is strongest in this pattern. Weak Great Lakes synoptic storms (perhaps related to shortwaves embedded in the upper-level flow), along with their attendant cold and warm fronts, are also associated with inland extremes. In

addition, some cold fronts may be associated with low-level thermal contrasts due to organized convection, or be extensions of cold fronts draped across the Northeast and originating from synoptic systems located well to the north of the region.

For the other patterns (the shallow trough/ridge, the eastern troughs, and the Ohio Valley troughs), the presence of nearby synoptic storms is critical to understanding the processes that lead to extreme precipitation. The warm-season trough/ridge pattern C4 appears to be related inland to ample moisture flow and moderate synoptic forcing associated with enhanced instability and a storm track to the west of the region. For the eastern troughs C2 and C5, dynamical lift is generated by quasi-geostrophic (QG) forcing, which is particularly strong for the wintertime C2 pattern. The C2 pattern appears to represent classic ‘nor’easter-type’ synoptic storms, with strong southerly flow of moisture up to 48 h before extreme events in the presence of WCBs just offshore; while the C5 pattern represents a warm-season shallow trough in nearly the same location, but with comparatively less moisture availability, and the strongest dynamical forcing mechanisms to the west in the form of cold fronts, and in Maine with warm fronts related to offshore WCBs. In contrast, the wintertime Ohio Valley troughs C3 and C6 represent storms travelling inland from the Atlantic seaboard through New England. Abundant moisture transported from the south ahead of the storms, and vigorous upward motion associated with the accompanying WCBs account for many

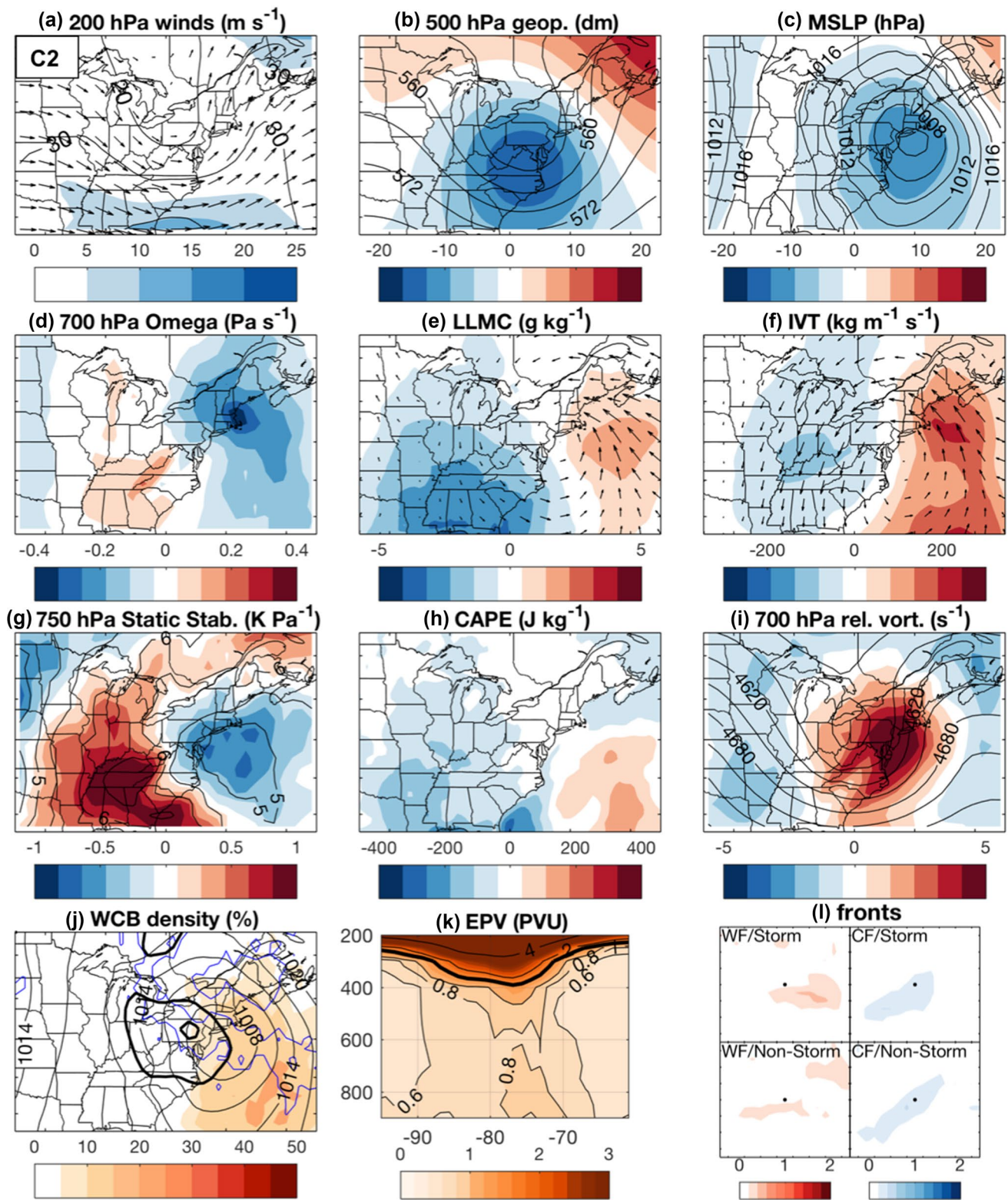


Fig. 7 Same as Fig. 2, but for eastern trough C2

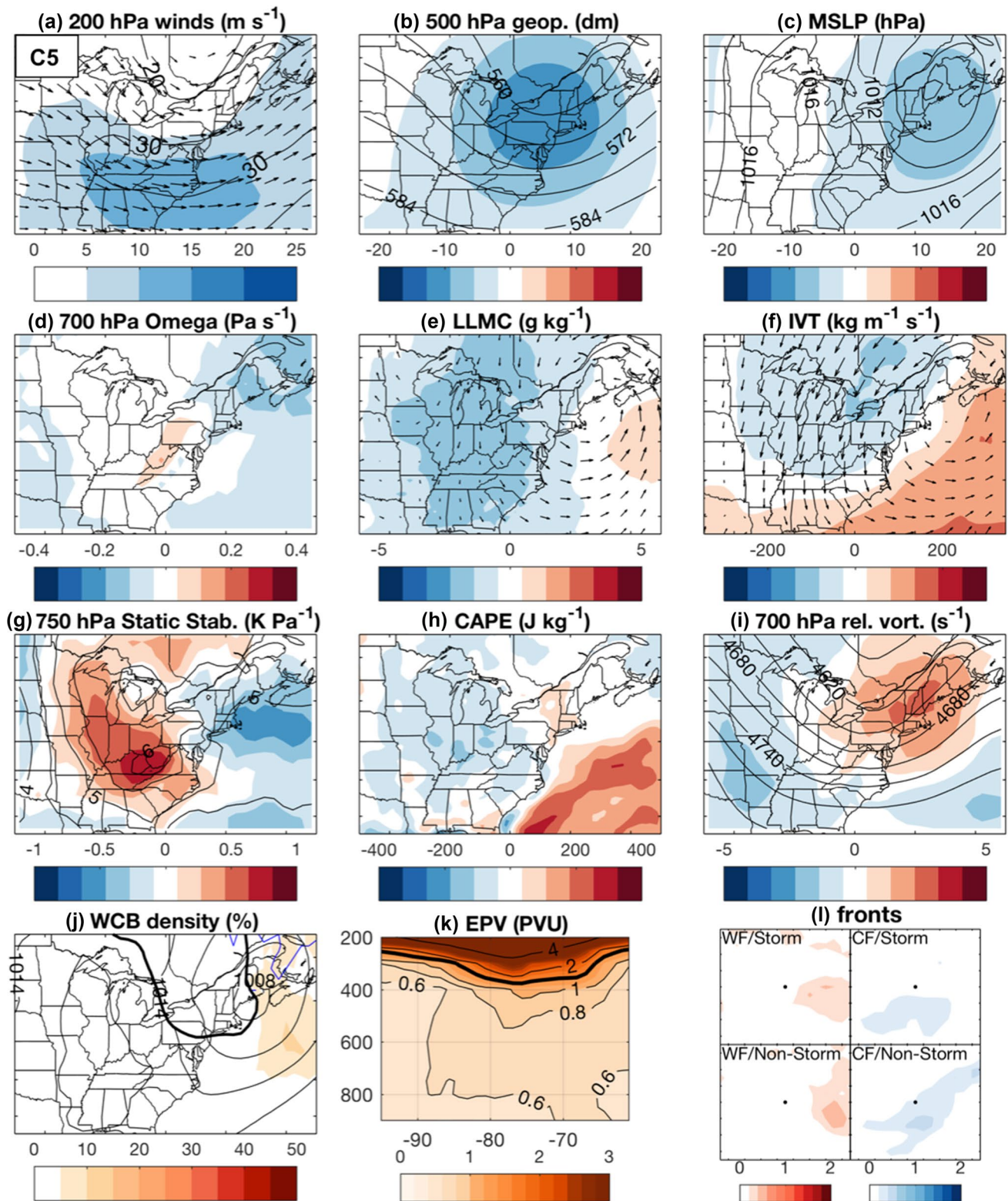


Fig. 8 Same as Fig. 2, but for eastern trough C5

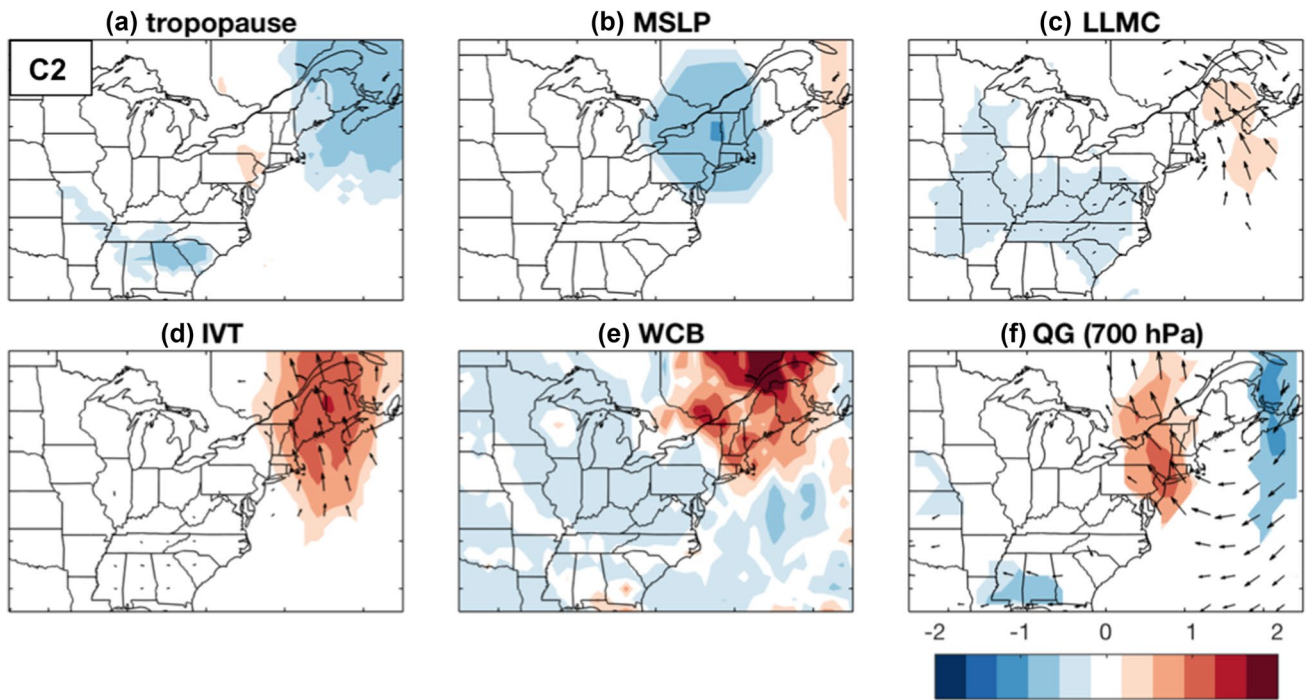


Fig. 9 Same as Fig. 4, but for SOM26 (similar to C2), and with \mathbf{f} thermal wind form of QG forcing, i.e. 700-hPa relative vorticity and 900–500 hPa thermal wind (arrows)

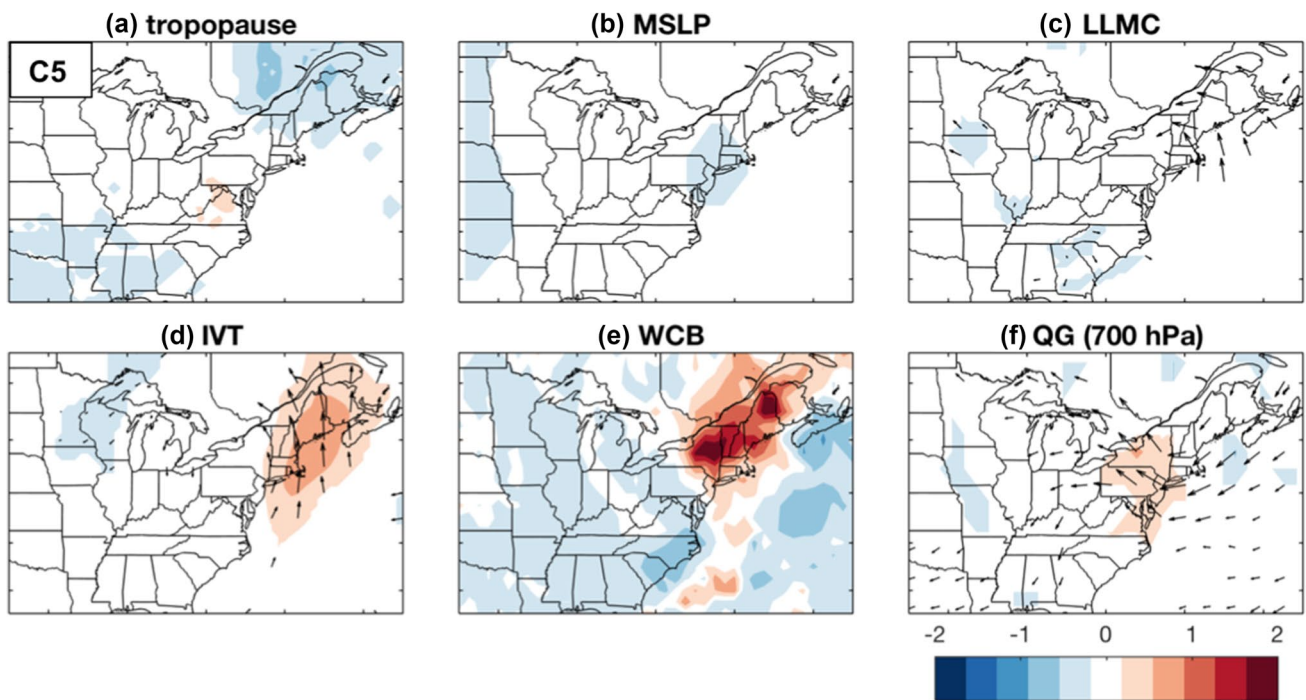


Fig. 10 Same as Fig. 9, but for SOM20 (similar to C5)

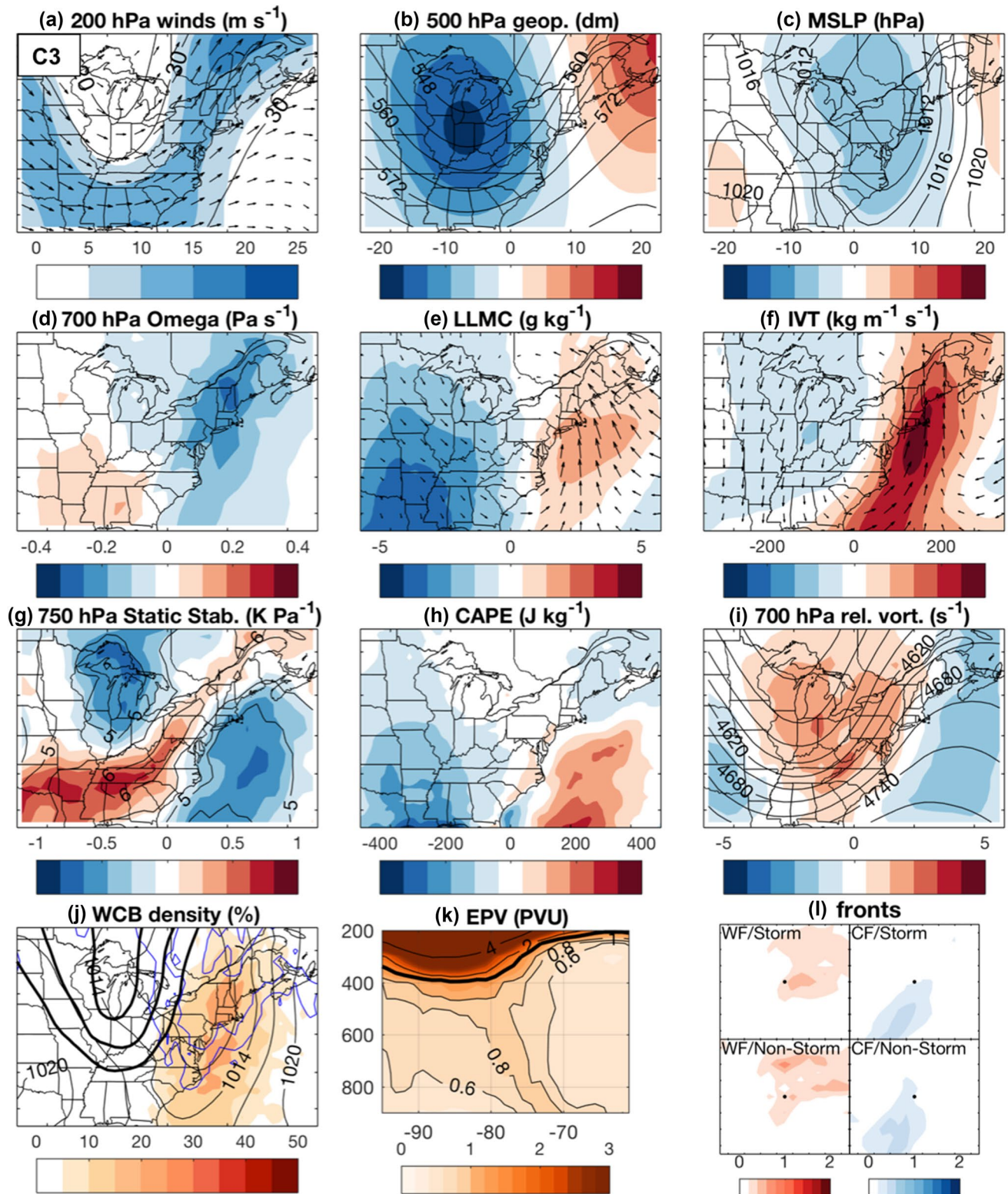


Fig. 11 Same as Fig. 2, but for Ohio Valley trough C3

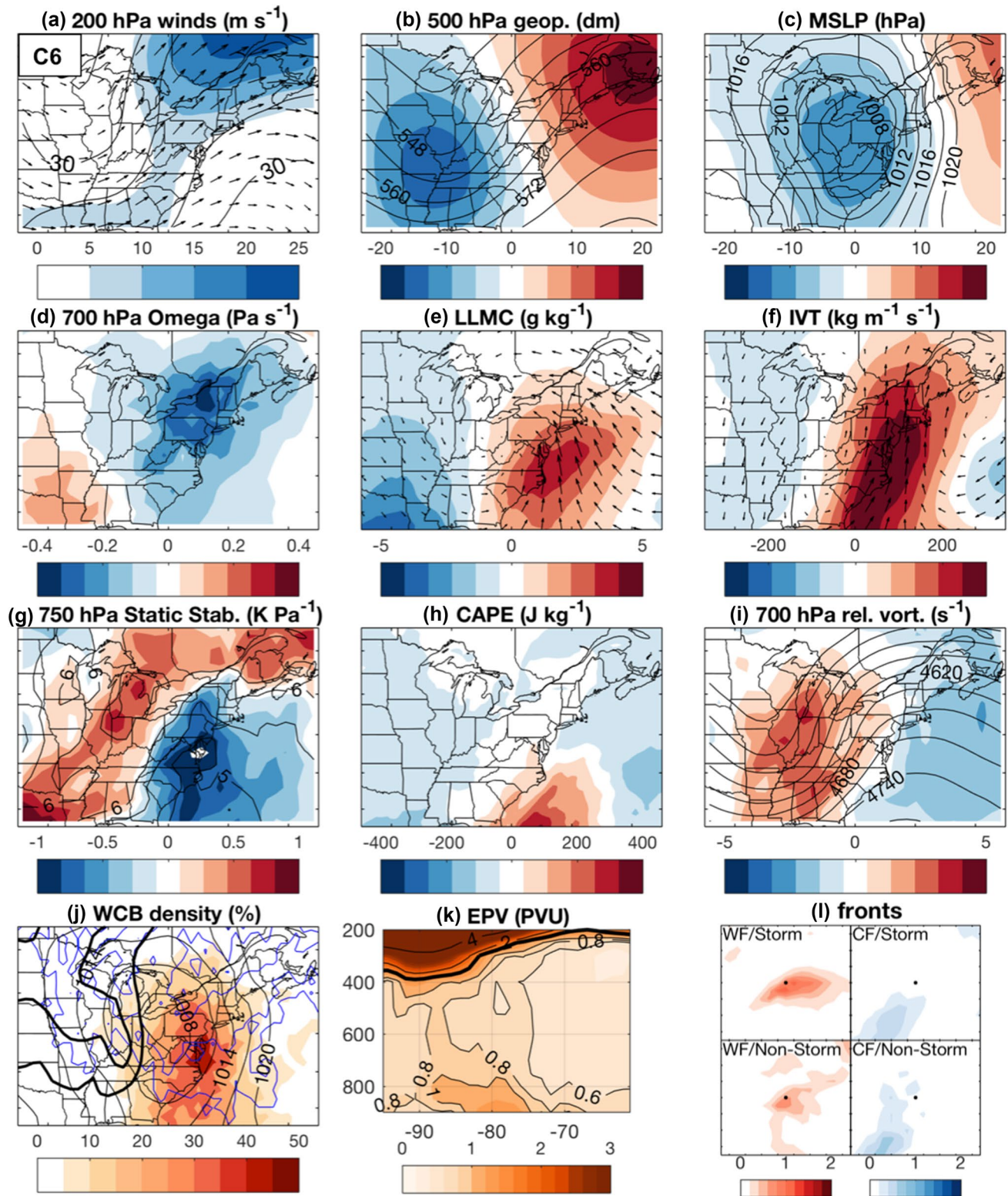


Fig. 12 Same as Fig. 2, but for Ohio Valley trough C6

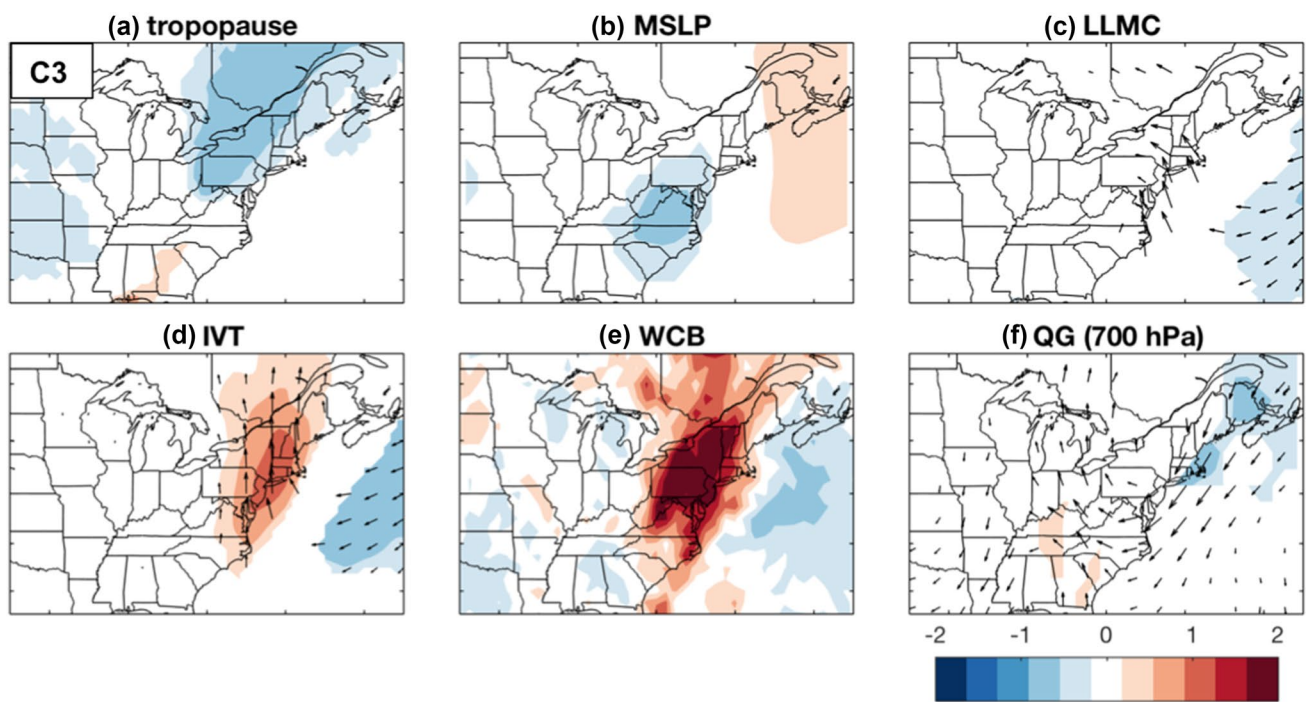


Fig. 13 Same as Fig. 9, but SOM13 (similar to C3)

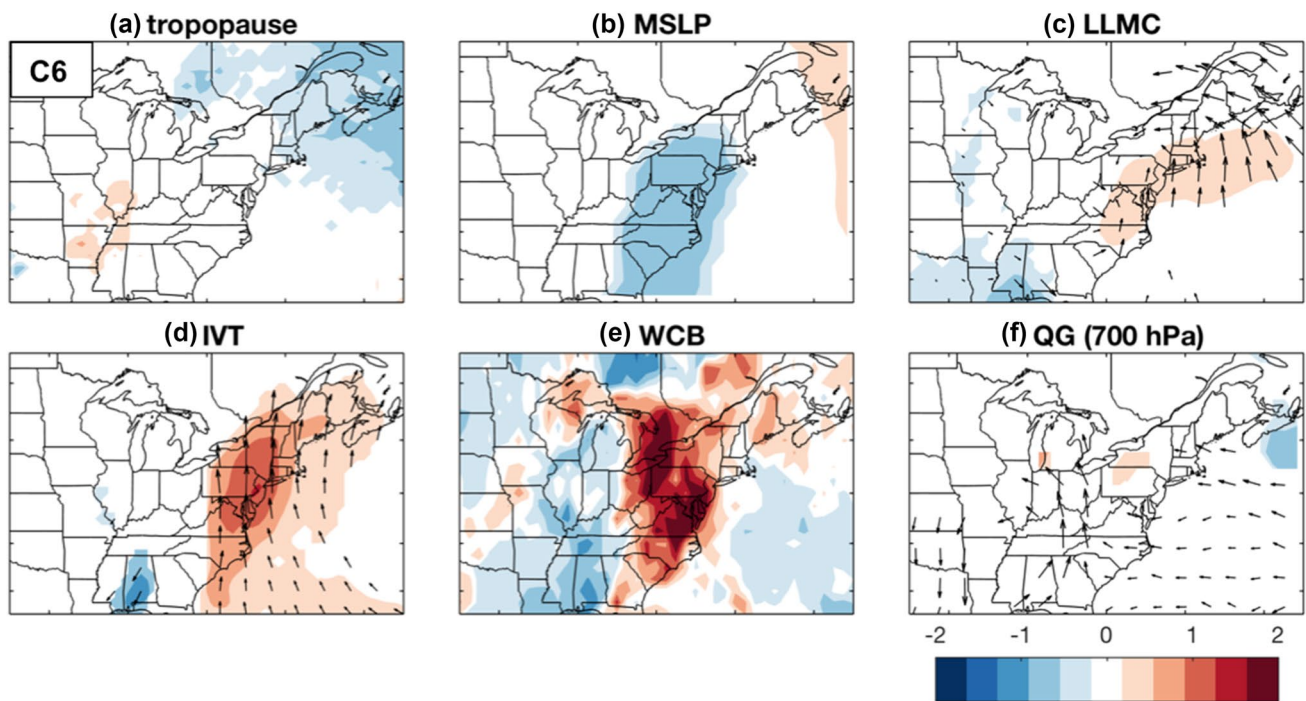


Fig. 14 Same as Fig. 9, but for SOM1 (similar to C6)

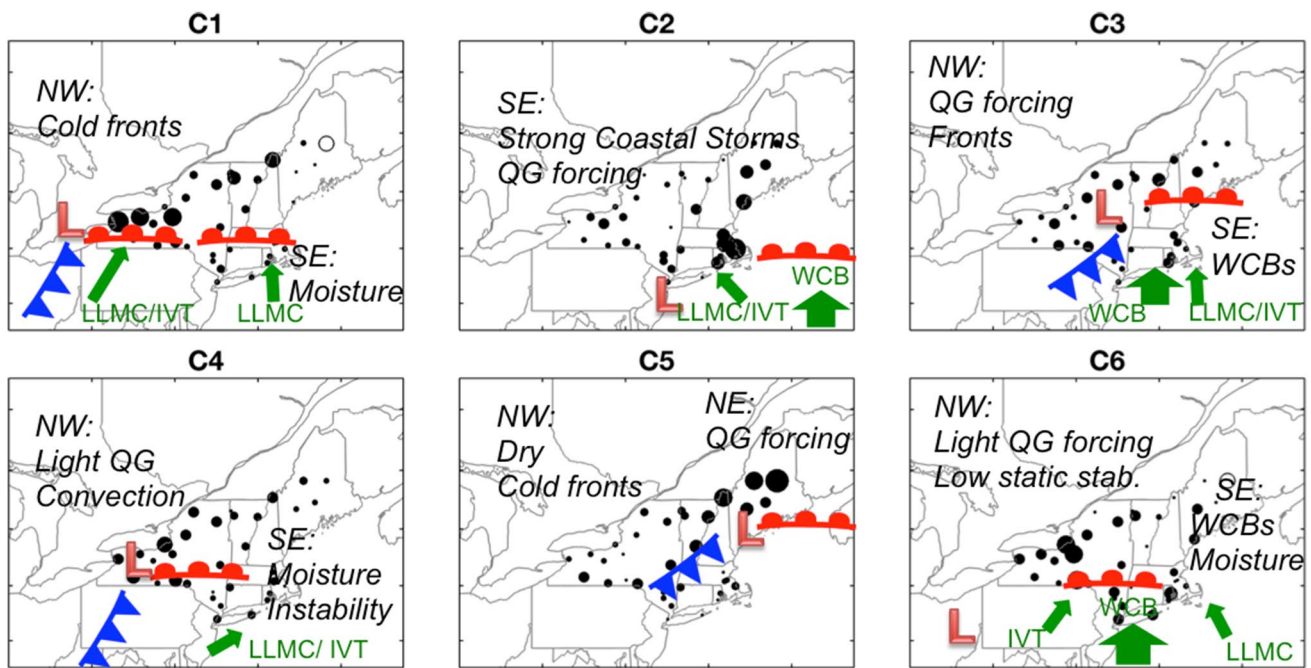


Fig. 15 Identification of key ingredients and processes linked to extreme precipitation for each of the k-means patterns C1–C6. Shown are dominant moisture processes (LLMC, IVT, WCBs; green arrows),

cold fronts, warm fronts, and low pressure centers (orange L symbol), and station locations experiencing extremes (black dots, with size of dot indicating relative frequency of extremes within pattern)

of the precipitation extremes in these patterns, with QG forcing linked to some extremes in western New York.

All patterns show stronger IVT on extreme precipitation days, with southerly anomalies for the eastern and Ohio Valley troughs, southwesterly anomalies for the trough/ridge C4 and near-westerly anomalies for ridge pattern C1. The IVT differences are among the largest magnitude differences between extreme and non-extreme days and indicate that moisture availability is a very important ingredient for extreme precipitation production in each pattern type. In addition, moisture transport tends to be more southerly on extreme days than for non-extreme days for each pattern type. By constructing a simple “IVT index” of standardized anomalies of mean IVT over a select area (38°N – 48°N , 82°W – 67°W), we find that 23.9% of extreme IVT days (defined here as 2.5+ standard anomalies) occur in conjunction with extreme precipitation, while 9.9% of extreme precipitation days involve extreme IVT. For pattern C6, this number is larger, with 27.5% of the extreme days featuring extreme IVT.

Equally important for generating extreme precipitation as opposed to ordinary precipitation within the trough patterns is the presence of WCBs. In fact, the differences of WCB frequency between extreme and non-extreme precipitation days for each of the patterns, including the ridge C1 and the shallow trough/ridge C4, are among the largest standardized differences for the patterns. To better quantify

the relationship between extreme precipitation and WCBs for the Northeast, we calculate the mean WCB frequency over the domain for each day containing at least one WCB, and define the top 10% as “high WCB frequency days”. We find that for Ohio Valley trough C6, 43.5% of extreme precipitation occurs on high WCB frequency days. For C2 and C3, the values drop to 25.6 and 20.6%, respectively, but are still considerably higher than that for the ridge patterns C1 (5%) and C4 (5.4%), and the summertime eastern trough C5 (2.5%). Tools such as the “IVT index” or “high WCB frequency days” can be valuable additions to the compositing techniques largely used here to identify the factors associated with extreme precipitation.

In this study we look at several upper-level patterns, or LSMPs, that occur during extreme precipitation events, and seek to understand how the key processes and ingredients for extreme precipitation (i.e. lift mechanisms, moisture, and instability) are informed by those patterns. Our approach focuses on composite representations of these factors. To the extent that individual pattern days share the same features as the composites, this provides a reasonable first-order assessment of what leads to extreme precipitation for various upper-level circulation patterns. However, individual events within each pattern type may yield quite different results. For example, for the summertime eastern trough C5, manual inspection reveals that some days feature large levels of instability, while others feature greater lift due to synoptic

QG forcing. An important next step is to investigate representative days within these pattern types for a more nuanced understanding of how extreme precipitation is generated, and to determine if the LSMPs can be further broken into representative sub-patterns. In addition, it is important to understand how these large-scale factors interact with sub-grid-scale processes. To this end, we intend to look more closely at the frontal processes (QG, slantwise instability, and other mesoscale dynamics) associated with extreme precipitation, which are best done by event, or within an event-centric framework. As a final step, we also intend to examine the explanatory power of the extreme precipitation factors identified here, perhaps through the use of simple predictive models and measures such as the “IVT index”.

Acknowledgements We are grateful to Heini Wernli (ETH Zurich) for his constructive comments and suggestions. Funding provided by National Science Foundation (NSF Project #1623912) to LA and MB. HB is supported by the Swiss National Science Foundation (SNSF) via Grants 200020_146834/P2EZP2_175161. JC is supported by the National Science Foundation Division of Polar Programs (Grant PLR-1504361) and the National Science Foundation Large-Scale and Climate Dynamics Program (Grants AGS-1657748).

References

- Agel L, Barlow M, Qian J-H, Colby F, Douglas E, Eichler T (2015) Climatology of daily precipitation and extreme precipitation events in the northeast United States. *J Hydrometeorol* 16:2537–2557. <https://doi.org/10.1175/JHM-D-14-0147.1>
- Agel L, Barlow M, Feldstein SB, Gutowski WJ (2017) Identification of large-scale meteorological patterns associated with extreme precipitation in the US northeast. *Clim Dyn*. <https://doi.org/10.1007/s00382-017-3724-8>
- Berry G, Jakob C, Reeder M (2011) Recent global trends in atmospheric fronts. *Geophys Res Lett* 38:L21812. <https://doi.org/10.1029/2011GL049481>
- Binder H, Boettcher M, Joos H, Wernli H (2016) The role of warm conveyor belts for the intensification of extratropical cyclones in Northern Hemisphere winter. *J Atmos Sci* 73:3997–4020. <https://doi.org/10.1175/jas-d-15-0302.1>
- Browning KA (1990) Organization of clouds and precipitation in extratropical cyclones. Extratropical cyclones: the Erik Palmén memorial volume. In: Newton CW, Holopainen EO (eds). American Meteorological Society, London, pp 129–153
- Catto JL, Pfahl S (2013) The importance of fronts for extreme precipitation. *J Geophys Res Atmos* 118:791–710,801. <https://doi.org/10.1002/jgrd.50852>
- Catto JL, Shaffrey LC, Hodges KI (2010) Can climate models capture the structure of extratropical cyclones? *J Clim* 23:1621–1635. <https://doi.org/10.1175/2009jcli3318.1>
- Catto JL, Jakob C, Berry G, Nicholls N (2012) Relating global precipitation to atmospheric fronts. *Geophys Res Lett* 39:L10805. <https://doi.org/10.1029/2012GL051736>
- Catto JL, Nicholls N, Jakob C, Shelton KL (2014) Atmospheric fronts in current and future climates. *Geophys Res Lett* 41:7642–7650. <https://doi.org/10.1002/2014GL061943>
- Catto JL, Madonna E, Joos H, Rudeva I, Simmonds I (2015) Global Relationship between fronts and warm conveyor belts and the impact on extreme precipitation. *J Clim* 28:8411–8429. <https://doi.org/10.1175/jcli-d-15-0171.1>
- Chen M, Xie P et al (2008) CPC unified gauge-based analysis of global daily precipitation. In: Western Pacific geophysics meeting, Cairns, Australia, 29 July–1 August 2008
- Collow ABM, Bosilovich MG, Koster RD (2016) Large-scale influences on summertime extreme precipitation in the northeastern United States. *J Hydrometeorol* 17:3045–3061. <https://doi.org/10.1175/jhm-d-16-0091.1>
- Dee DP et al (2011) The ERA-Interim reanalysis: configuration and performance of the data assimilation system. *Q J R Meteorol Soc* 137:553–597. <https://doi.org/10.1002/qj.828>
- Diday E, Simon JC (1976) Clustering analysis. In: Fu KS (ed) Digital pattern recognition. Springer, Berlin, pp 47–94. https://doi.org/10.1007/978-3-642-96303-2_3
- Dowdy AJ, Catto JL (2017) Extreme weather caused by concurrent cyclone, front and thunderstorm occurrences. *Sci Rep* 7:40359. <https://doi.org/10.1038/srep40359>. <https://www.nature.com/articles/srep40359#supplementary-information>
- Easterling DR, Karl TR, Lawrimore JH, Del Greco SA (1999) United states historical climatology network daily temperature, precipitation, and snow data for 1871–1997. Carbon Dioxide Information Analysis Center, Oak Ridge National Laboratory, US Department of Energy, Oak Ridge, TN. <https://digital.library.unt.edu/ark:/67531/metadc735162/ORNL/CDIAC-118>, <http://cdiac.esd.ornl.gov/epubs/ndp/usnhc/ndp070.html>
- Glisan JM, Gutowski WJ (2014) WRF winter extreme daily precipitation over the North American CORDEX Arctic. *J Geophys Res Atmos* 119:10738–10748. <https://doi.org/10.1002/2014JD021676>
- Grams CM et al (2011) The key role of diabatic processes in modifying the upper-tropospheric wave guide: a North Atlantic case-study. *Q J R Meteorol Soc* 137:2174–2193. <https://doi.org/10.1002/qj.891>
- Green JSA, Ludlam HF, McIlveen JFR (1966) Isentropic relative-flow analysis and the parcel theory. *Q J R Meteorol Soc* 92(392):210–219. <https://doi.org/10.1002/qj.49709239204>
- Groisman PY, Knight RW, Zolina OG (2013) Recent trends in regional and global extreme precipitation patterns. In: Sr RP, Hossain F (eds) Climate vulnerability: understanding and addressing threats to essential resources. Volume 5, vulnerability of water resources to climate. Elsevier Publishing House, Amsterdam, pp 25–55
- Grotjahn R et al (2016) North American extreme temperature events and related large scale meteorological patterns: a review of statistical methods, dynamics, modeling, and trends. *Clim Dyn* 46:1151–1184. <https://doi.org/10.1007/s00382-015-2638-6>
- Harrold TW (1973) Mechanisms influencing the distribution of precipitation within baroclinic disturbances. *Q J R Meteorol Soc* 99:232–251. <https://doi.org/10.1002/qj.49709942003>
- Hewson TD (1998) Objective fronts. *Meteorol Appl* 5:37–65. <https://doi.org/10.1017/S1350482798000553>
- Holton JR (2004) An introduction to dynamic meteorology, 4th edn. Elsevier Academic Press, Massachusetts
- Hoskins BJ, Hodges KI (2002) New perspectives on the northern hemisphere winter storm tracks. *J Atmos Sci* 59:1041–1061. [https://doi.org/10.1175/1520-0469\(2002\)059<1041:npotnh>2.0.co;2](https://doi.org/10.1175/1520-0469(2002)059<1041:npotnh>2.0.co;2)
- Hoskins BJ, McIntyre ME, Robertson AW (1985) On the use and significance of isentropic potential vorticity maps. *Q J R Meteorol Soc* 111:877–946. <https://doi.org/10.1002/qj.49711147002>
- Kocin PJ, Uccellini LW (2004) Volume I: overview. Meteorological monographs, vol 54. American Meteor Society, pp 1–270
- Kohonen T (2001) Self-organizing maps. Springer, New York
- Kunkel KE, Easterling DR, Kristovich DAR, Gleason B, Stoecker L, Smith R (2012) Meteorological causes of the secular variations in observed extreme precipitation events for the conterminous United States. *J Hydrometeorol* 13:1131–1141. <https://doi.org/10.1175/jhm-d-11-0108.1>

- Kunkel K et al (2013) Regional climate trends and scenarios for the U.S. national climate assessment. Part 1. Climate of the northeast U.S. NOAA Technical Report NESDIS 142-1, pp 80
- Landsea CW, Franklin JL (2013) Atlantic hurricane database uncertainty and presentation of a new database format. *Mon Weather Rev* 141:3576–3592. <https://doi.org/10.1175/MWR-D-12-00254.1>
- Loikith PC, Broccoli AJ (2012) Characteristics of observed atmospheric circulation patterns associated with temperature extremes over North America. *J Clim* 25:7266–7281. <https://doi.org/10.1175/jcli-d-11-00709.1>
- Madonna E, Wernli H, Joos H, Martius O (2014) Warm conveyor belts in the ERA-interim dataset (1979–2010). Part I: climatology and potential vorticity evolution. *J Clim* 27:3–26. <https://doi.org/10.1175/JCLI-D-12-00720.1>
- Maglaras GJ, Waldstreicher JS, Kocin PJ, Gigi AF, Marine RA (1995) Winter weather forecasting throughout the eastern United States. Part I: an overview. *Weather Forecast* 10:5–20 [https://doi.org/10.1175/1520-0434\(1995\)010<0005:WWFTTE>2.0.CO;2](https://doi.org/10.1175/1520-0434(1995)010<0005:WWFTTE>2.0.CO;2)
- Melillo JM, Richmond TC, Yohe GW (2014) Climate change impacts in the United States: the third national climate assessment. US Global Change Research Program, pp 841. <https://doi.org/10.7930/J0Z31WJ2>
- Michelangeli P-A, Vautard R, Legras B (1995) Weather regimes: recurrence and quasi stationarity. *J Atmos Sci* 52:1237–1256. [https://doi.org/10.1175/1520-0469\(1995\)052<1237:WRRASQ>2.0.CO;2](https://doi.org/10.1175/1520-0469(1995)052<1237:WRRASQ>2.0.CO;2)
- Milrad SM, Atallah EH, Gyakum JR, Dookhie G (2014) Synoptic typing and precursors of heavy warm-season precipitation events at Montreal, Québec. *Weather Forecast* 29:419–444. <https://doi.org/10.1175/WAF-D-13-00030.1>
- Muller CJ, O’Gorman PA, Back LE (2011) Intensification of precipitation extremes with warming in a cloud-resolving model. *J Clim* 24:2784–2800
- Nielsen-Gammon JW (2001) A Visualization of the Global Dynamic Tropopause. *Bull Am Meteorol Soc* 82:1151–1167. [https://doi.org/10.1175/1520-0477\(2001\)082<1151:AVOTGD>2.3.CO;2](https://doi.org/10.1175/1520-0477(2001)082<1151:AVOTGD>2.3.CO;2)
- Pfahl S, Sprenger M (2016) On the relationship between extratropical cyclone precipitation and intensity. *Geophys Res Lett* 43:1752–1758. <https://doi.org/10.1002/2016GL068018>
- Pfahl S, Wernli H (2012) Quantifying the relevance of cyclones for precipitation extremes. *J Clim* 25:6770–6780. <https://doi.org/10.1175/jcli-d-11-00705.1>
- Pfahl S, Madonna E, Boettcher M, Joos H, Wernli H (2014) Warm Conveyor belts in the ERA-interim dataset (1979–2010). Part II: moisture origin and relevance for precipitation. *J Clim* 27:27–40. <https://doi.org/10.1175/JCLI-D-13-00223.1>
- Pomroy HR, Thorpe AJ (2000) The evolution and dynamical role of reduced upper-tropospheric potential vorticity in intensive observing period one of FASTEX. *Mon Weather Rev* 128:1817–1834. [https://doi.org/10.1175/1520-0493\(2000\)128<1817:teadro>2.0.co;2](https://doi.org/10.1175/1520-0493(2000)128<1817:teadro>2.0.co;2)
- Rienecker MM et al (2011) MERRA: NASA’s modern-era retrospective analysis for research and applications. *J Clim* 24:3624–3648. <https://doi.org/10.1175/jcli-d-11-00015.1>
- Roller CD, Qian J-H, Agel L, Barlow M, Moron V (2016) Winter weather regimes in the northeast United States. *J Clim* 29:2963–2980. <https://doi.org/10.1175/JCLI-D-15-0274.1>
- Saha S et al (2010) The NCEP climate forecast system reanalysis. *Bull Am Meteor Soc* 91:1015–1058. <https://doi.org/10.1175/2010bams3001.1>
- Schumacher RS, Johnson RH (2005) Organization and environmental properties of extreme-rain-producing mesoscale convective systems. *Mon Weather Rev* 133:961–976. <https://doi.org/10.1175/MWR2899.1>
- Sprenger M, Wernli H (2015) The LAGRANTO Lagrangian analysis tool—version 2.0. 8. <https://doi.org/10.5194/gmd-8-2569-2015>
- Stoelinga MT (1996) A potential vorticity-based study of the role of diabatic heating and friction in a numerically simulated baroclinic cyclone. *Mon Weather Rev* 124:849–874. [https://doi.org/10.1175/1520-0493\(1996\)124<0849:apvbs>2.0.co;2](https://doi.org/10.1175/1520-0493(1996)124<0849:apvbs>2.0.co;2)
- Wernli H (1997) A Lagrangian-based analysis of extratropical cyclones. II: a detailed case-study. *Q J R Meteorol Soc* 123:1677–1706. <https://doi.org/10.1002/qj.49712354211>
- Wernli H, Davies HC (1997) A lagrangian-based analysis of extratropical cyclones. I: the method and some applications. *Q J R Meteorol Soc* 123:467–489. <https://doi.org/10.1002/qj.49712353811>